Evaluation of Sc concentrations in Ni-Co laterites using Al as a geochemical proxy

Yoram Teitler, Sylvain Favier, Jean-Paul Ambrosi, Brice Sevin, Fabrice Golfier, Michel Cathelineau

Evaluation of Sc concentrations in Ni-Co laterites using Al as a geochemical proxy

Y. TEITLER[1]*, S. FAVIER[1], J.P. AMBROSI[2], B. SEVIN[3], F. GOLFIER[1], M. CATHELINEAU[1]

[1] Université de Lorraine, CNRS, GeoRessources, 54000 Nancy, France

[2] Aix-Marseille Université, CNRS, IRD, INRAE, CEREGE, Aix-en-Provence, France

[3] Service de la Géologie de Nouvelle-Calédonie, Direction de l'industrie, des Mines et de l'Énergie, 1ter rue Unger, BP M2, 98849 Nouméa Cedex, New Caledonia

*yoram.teitler@univ-lorraine.fr

Declarations of interest: none

Keywords

Scandium; laterite; Ni-laterite; sequential extraction; New Caledonia

Abstract

Scandium (Sc) is used in several modern industrial applications, including aluminium-based alloys and solid oxide fuel cells. So far, Sc production remains marginal as the lack of reliable and cost-effective production limits its widespread adoption by the industry. Recently, significant Sc concentrations (~100 ppm) were reported in some nickel-cobalt lateritic ores, where Sc may be valuably co-produced along with Ni and Co. However, Sc is typically not included in routine analyses of Ni-Co ores, precluding the assessment of Sc concentration and distribution in existing Ni-Co deposits. This contribution examines the relevance of using routinely analysed elements as geochemical proxies for providing first-order estimates of Sc concentration and distribution in already assayed Ni-Co deposits. Three Ni-Co lateritic deposits from New Caledonia, developed after harzburgite (Ma-Oui deposit, Koniambo mine), harzburgite-dunite (Coquette Red tenement, Cap Bocage mine) and lherzolite (East Alpha deposit, Tiébaghi mine), were investigated. In each deposit, we demonstrate that Sc is globally well correlated with Al_2O_3, providing that the parent lithology is homogeneous and relatively depleted in Al. Deposit-

scale Sc-Al_2O_3 regression lines are remarkably controlled by the composition of enstatite from the parent rock. In all deposits, zones of maximum Sc enrichment are situated in the yellow limonite, above the zones of highest Ni and Co enrichments. Sequential extractions highlight that Sc- and Al-bearing crystalline goethite is predominant, though Sc shows a higher affinity for amorphous iron oxides than Al. We propose that, in already assayed Ni-Co lateritic ores, the concentration and distribution of Sc can be estimated from that of Al, assuming that the Sc-Al_2O_3 correlation is valid at the deposit scale. Such deposit-scale correlations may be determined after analysing a limited number of spatially and chemically representative samples. Therefore, mining operators may get a first-order evaluation of the Sc potential resource in Ni-Co lateritic deposits at low additional costs.

1 Introduction

Scandium (Sc) is mainly used as a hardening additive to aluminium to form Al-Sc alloys for aerospace industries and manufacture of high-quality sports equipment (Royset and Ryum, 2005; Toropova et al., 1998). In addition, Sc is notably used in high-temperature lights, lasers and ceramics manufacturing and finds promising application in the development of Solid Oxide Fuel Cells (SOFCs). The global Sc supply and consumption remain marginal (~15 to 25t/yr Sc_2O_3, US Geological Survey, 2022). Sc is solely recovered as a by-product through titanium, zirconium, uranium, cobalt and nickel process streams. Nevertheless, the development of energy-saving technologies and Sc extraction techniques have raised interest in this metal. In the last decade, Sc-rich occurrences with economically attractive grades and tonnages have been identified in some oxide-rich laterites developed after mafic and ultramafic rocks (Aiglsperger et al., 2016; Audet, 2008; Bailly et al., 2014; Chassé et al., 2017, 2019; Hoatson et al., 2011; Maulana et al., 2016; Qin et al., 2020; Sun et al., 2021; Teitler et al., 2019; Ulrich et al., 2019). There, Sc enrichment is largely residual and results from the intense leaching of mobile cations during the lateritisation of the parent rock. Scandium is thus trapped and concentrated in neo-formed goethite, and moderate remobilisation can occur during repeated stages of goethite dissolution-recrystallisation and transformation into hematite. The chemical speciation of Sc in laterites from

55 Australia and the Philippines has been investigated using a combination of X-ray absorption near-edge
56 structure (XANES) spectroscopy and sequential extractions (Chassé et al., 2017, 2019; Qin et al., 2020).
57 These studies further support the preferential affinity of Sc for goethite compared to hematite or
58 smectite. However, the relative importance of adsorption and incorporation processes and the impact
59 of goethite crystallinity in the formation of Sc-rich goethite zones remain debated. They may vary from
60 one deposit to another. In New Caledonia, significant Sc concentrations were reported in several Ni-
61 Co lateritic oxide ores (Teitler et al., 2019; Ulrich et al., 2019). There, maximum Sc grades reach ~100
62 ppm in the yellow limonite horizon. Although such concentrations are too low to be economically
63 attractive as primary resources, Sc could be a valuable by-product of Ni and Co processing, provided
64 that Sc-rich zones sufficiently overlap Ni- and Co-rich zones (Teitler et al., 2019). However, Sc is typically
65 not routinely analysed during exploration and resource estimation of Ni-Co laterites. Consequently,
66 mining operators do not evaluate the potential Sc resources hosted in Ni-Co lateritic ores.
67 In contrast, Fe, Al and Cr are routinely analysed and could serve as geochemical proxies for inferring
68 the distribution of Sc concentrations in lateritic Ni-Co ores as suggested by previous investigations
69 (Teitler et al., 2019). Although Fe is the predominant constituent of lateritic oxide ores with up to 80
70 wt% Fe_2O_3, Teitler et al. (2019) suggested that Fe may be correlated to Sc only in the lower to
71 intermediate sections of the lateritic profiles and that the Sc-Fe_2O_3 correlation is usually not valid in
72 the Sc-rich, yellow limonite horizon. In contrast, Sc is better correlated with Al in all the facies of the
73 lateritic profiles, except for the uppermost ferruginous duricrust.
74 Nevertheless, the Sc-Al_2O_3 correlation proposed by Teitler et al. (2019), based on the combined
75 analysis of individual vertical profiles from several deposits, shows significant dispersion and does not
76 allow to assess how reliable the Sc-Al_2O_3 proxy is at the deposit scale. In this contribution, we discuss
77 the relevance of the Sc-Al_2O_3, Sc-Fe_2O_3 and Sc-Cr_2O_3 correlations at the deposit scale in three Ni-Co
78 deposits from the Koniambo, Cap Bocage and Tiébaghi mines, New Caledonia, based on the
79 geochemical analysis of spatially and lithologically representative samples from each deposit. Using
80 laser ablation inductively coupled mass spectroscopy (LA-ICP-MS), we then examine the dependency

of bedrock mineral compositions on the Sc-Al_2O_3 regression coefficients and the variability of Al and Sc contents in secondary-formed minerals. Third, we conduct selective chemical leaching on some Sc-bearing samples to provide further insights on the speciation of Sc in the investigated deposits. These results are used to discuss the potential of the Al proxy for the evaluation of Sc concentrations and distribution in peridotite-hosted laterites in the perspective of Ni-Co-Sc co-valorisation.

2 Regional geology

The "Grande Terre" island of New Caledonia (Fig. 1A) consists of a 300 km long allochthonous peridotite ophiolite referred to as the "Peridotite Nappe". The peridotite Nappe, formed at ca. 35 Ma (Cluzel et al., 2001, 2012; Paquette and Cluzel, 2007), represents about 30% of the surface of Grande Terre and is exposed in the "Massif du Sud" and several isolated tectonic klippes, mainly aligned in the N140° direction along the west coast of the island (Koniambo, Tiebaghi, Poum massifs). The Peridotite Nappe is primarily composed of harzburgite locally interlayered with dunite, except in the northernmost klippes where lherzolite dominates (Ulrich et al., 2010). Notably, the extensive lateritisation of the peridotite ophiolite during or soon after obduction led to the development of a thick regolith cover and the formation of world-class Ni-Co(-Sc) lateritic resources representing about 10% of the world's nickel reserves (Maurizot et al., 2020). The development of Ni-Co(-Sc) laterites in New Caledonia results from (i) the leaching of most cations including Mg and Si after hydrolysis of olivine and pyroxene, (ii) the redistribution and concentration of Ni within the saprock as secondary hydrous silicates, (iii) the development of Ni-bearing saprolite, containing both silicates and oxides, at the expense of the saprock, and (iv) the development of oxide-rich, Ni-bearing limonite and duricrust at the expense of the saprolite (Butt and Cluzel, 2013; Cathelineau et al., 2016, 2017; Freyssinet et al., 2005; Golightly, 2010; Manceau et al., 2000; Trescases, 1975; Wells et al., 2009). The Ni-rich (> 2.0 wt% Ni) Ni-silicates ore reserves are rapidly being depleted as they have been actively mined since the late 19th century. Lower-grade (1.0–2.0% Ni) oxide ore ("limonite") reserves will therefore represent the bulk of Ni reserves of New Caledonia in the future. Also, Ni oxide ores often yield elevated Co (>2000

ppm) and Sc (60-100 ppm) concentrations adding significant value to the ore (Fig. 1B). Maximum Co concentrations (> 2000 ppm) typically occur at the interface between saprolite and limonite (referred to as transition zone), where Co is mainly associated with Mn-oxides (e.g. asbolane, lithiophorite). Upwards in the limonitic horizons, Co concentrations decrease being partially scavenged and trapped in ochreous goethite (Dublet et al., 2017). Maximum Sc grades are reached in the yellow limonite horizon (Fig. 1B). Therefore, Ni-, Co- and Sc-rich zones in limonite may partly overlap each other, and the degree of such overlap is critical in the perspective of co-valorising Ni, Co and Sc from lateritic Ni ores.

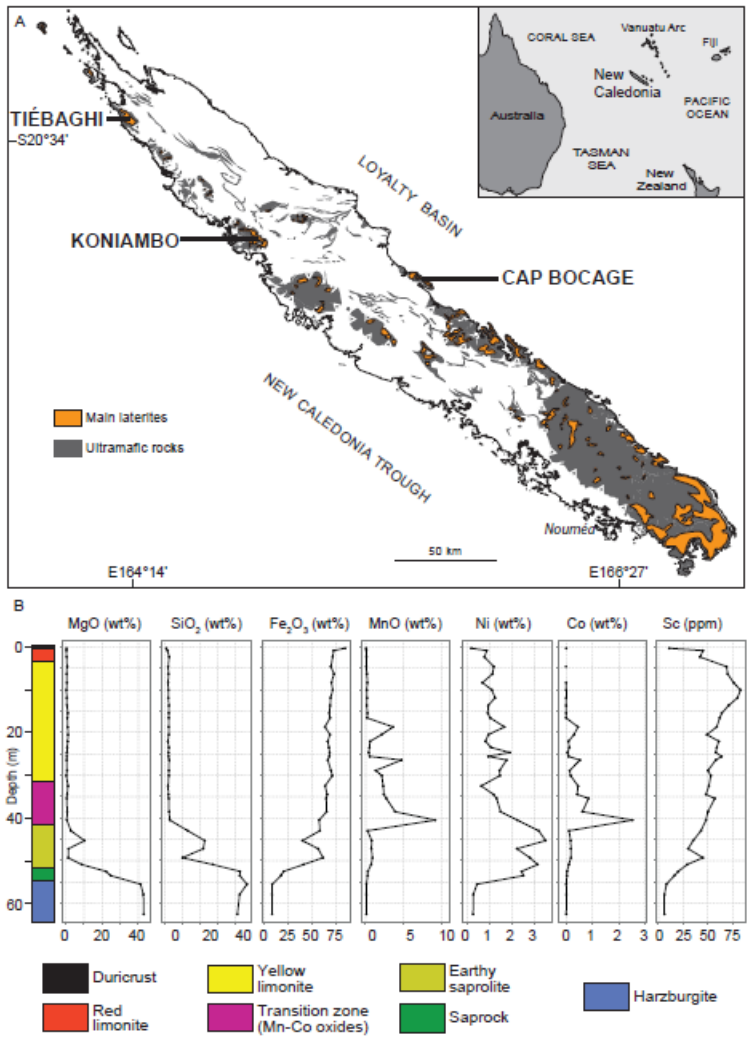

Fig. 1: (A) Geological map of New Caledonia and location of the investigated mine sites. Modified from Maurizot and Vendé-Leclerc (2009). (B) Geochemical evolution along a typical Ni-lateritic profile in New Caledonia (modified from Bailly et al., 2014).

3 Methodology

3.1 Sampling strategy

Sampling was conducted in multiple locations within the investigated deposits, along several drillcores and pit walls, encompassing the diversity of representative lithofacies. The objective was to check whether Sc-Al_2O_3 correlations may be generalised at the deposit scale. At the Ma-Oui deposit (Koniambo), 39 samples were collected along 6 drillcores and one pit wall profile (Fig. 2A). At the Coquette Red tenement (Cap Bocage), 27 samples were collected along 2 drillcores and one outcrop profile (Fig. 2B). At the East Alpha deposit (Tiébaghi), 48 samples were collected along 9 pit wall profiles, including one located in saprolite formed after gabbro (Fig. 2C).

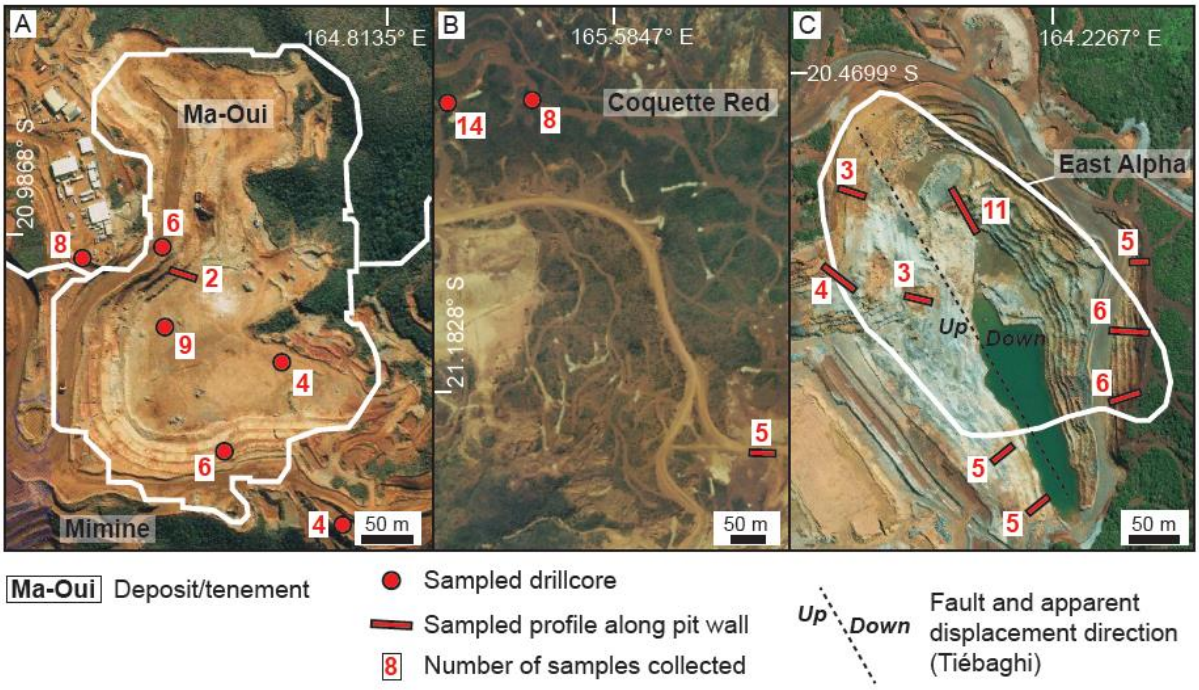

Fig. 2: Outline of the investigated deposits and location of collected samples. (A) Ma-Oui deposit (Koniambo). (B) Coquette Red tenement (Cap Bocage). (C) East Alpha deposit (Tiébaghi).

3.2 Analytical strategy

Among the 114 samples collected for whole-rock geochemical analysis, 49 samples (batch 1) were analysed at the SARM analytical service of the CRPG (France), and 65 samples (batch 2) were analysed at the NILAB laboratory (New Caledonia). Sixteen thin polished sections were prepared and examined using reflected/transmitted light and scanning electron microscopy with a JEOL JSM7600F at Georessources Laboratory and SCMEM. *In situ* mineral chemistry analysis for major/minor elements (Mg, Al, Si, Ca, Cr, Mn, Fe, Co, Ni) was conducted using a CAMECA SX100 electron microprobe (EPMA, WDS analysis) at the SCMEM with typical beam conditions of 15 kV and 10 nA. *In situ* analysis for Sc and minor/trace elements was conducted using LA-ICP-MS (193 nm MicroLas ArF Excimer coupled with Agilent 7500c quadrupole ICP-MS). Sequential extractions were performed at the CEREGE laboratory on seven Sc-bearing samples from Cap Bocage and Tiébaghi. Four reagents were successively used to extract major and trace elements selectively: (i) ultrapure water for easily soluble elements, (ii) 0.1 $mol.L^{-1}$ hydroxylamine hydrochloride NH_2OH-HCl at pH = 3.5, which is particularly efficient and selective for manganiferous phases, (iii) 0.2 $mol.L^{-1}$ ammonium oxalate $(NH_4)_2C_2O_4$ at pH = 3 for amorphous and poorly crystallised iron oxides and (iv) citrate-bicarbonate-dithionite $Na_2S_2O_4$ (22% Na-citrate and 1 g Na-dithionite) for well-crystallised iron oxides (Bailly et al., 2014). Additional information on analytical procedures and PCA are given in Appendix A.

4 Lithofacies and mineral assemblages

Progressive weathering of peridotite involves hydration and hydrolysis of primary silicates and the formation of secondary silicates and oxides-oxyhydroxides. Therefore, the investigated Ni-Co deposits exhibit a continuum of alteration facies with specific mineral assemblages and textures. At Koniambo and Cap Bocage, moderately serpentinised harzburgite represents the predominant parent rock of Ni-Co laterites (Fig. 3A, 4). It is worth noting that the Coquette Red tenement investigated at Cap Bocage hosts significant volumes of dunite lenses so that the lateritic profiles are developed both on

harzburgite and dunite. Serpentinisation occurs within the peridotite as mm to dm-large veins of serpentine (mostly lizardite) distributed as fracture networks and progressively replacing mantle silicates resulting in a typical mesh texture (Fig. 3A, 3C, 5A, 6A). At Tiébaghi, lherzolite dominates over harzburgite, although the intensive serpentinisation of the peridotite complicates its univocal recognition in the field. In the saprock, weathering initiates through the progression of the mantle silicate alteration front, marked by the onset of forsterite and enstatite hydrolysis (Fig. 5A, 6A) and the development of Ni-rich (up to 15–20 wt% Ni), greenish talc-like (kerolite) veins that root into the unweathered peridotite (Fig. 3C, 5A, 6A). Congruent hydrolysis of mantle silicate leads to the formation of 100-micron large pores with the development of skeletal goethite along silicate grain boundaries and crystallographic planes. Serpentine veins and mesh are preserved from dissolution in the saprock, although partly transformed into secondary, nickeliferous serpentine/talc-like (Fig. 5A, 5B). At Koniambo and Cap Bocage, local evidence for incongruent hydrolysis and epigenetic replacement of mantle silicate by smectite is also observed but is spatially restricted to the bedrock-saprock interface (Fig. 6A, 6C). There, epigenetic smectite is, in turn, readily replaced (e.g. by Mn-Co-Ni-rich lithiophorite, Fig. 6C) or dissolved and does not occur upwards in the profile. The evolution from the saprock to the saprolite, wherein weathering is more pronounced but remains isovolumetric, is characterised by the complete disappearance of mantle silicate and the partial replacement of serpentines by goethite (Fig. 3B, 5B, 6D). In contrast, at Tiébaghi, smectite extensively develops at the expense of both mantle silicates and serpentine (Fig. 3E, 4, 5C, 6B) and remains preserved throughout most of the saprolite until it is eventually replaced by ochreous goethite (Fig. 5D). The interface between the saprolite and the overlying limonite, referred to as the transition zone, is marked by the progressive disappearance of macroscopic primary structures and the accumulation of Mn-Co-Ni oxides (lithiophorite, asbolane) either as mm- to cm-thick veins or as diffuse accumulations in the iron-rich matrix (Fig. 3D). Upwards, the transition zone evolves into the yellow limonite wherein ochreous goethite predominates, characterised by the disappearance of all primary minerals except chromiferous spinel that remains mostly resistant to weathering throughout the entire profile. This horizon is marked by significant

compaction. However, primary textures such as fragmented relics of serpentine veins or skeletons of mantle silicates, both replaced by goethite, may still be recognised at the microscopic scale (Fig. 5E, 6E). The yellow limonite then grades into the red limonite, wherein hematite forms at the expense of ochreous goethite resulting in a mineral assemblage dominated by goethite but containing significant amounts (> 5 vol%) of hematite (Fig. 5F). Lateritic profiles are capped by a ferruginous duricrust that is either directly developed after the underlying limonite or derived from the ferrugination of transported material (Fig. 5G, 5H). Following the terminology of Anand et al. (2002), the term duricrust describes regolith materials cemented by Fe, irrespective of the substrate origin. When it is residual, the iron-cemented material is called a lateritic residuum, and when it is formed and indurated in a transported cover, ferricrete. Lateritic residuum exhibits, at the microscopic scale, some locally preserved textural relics (Fig. 6F). There, both goethite and hematite are largely recrystallised into coarser crystallites. In contrast, ferricrete shows angular goethite and hematite nodules with goethite pisolitic envelopes. They are cemented by vitreous goethite (Fig. 6G). Subvertical dykes of amphibolitic gabbros locally exposed in the East Alpha deposit, Tiébaghi, alter to form a mineral assemblage composed of kaolinite-gibbsite-hematite (Fig. 3F, 6H, 6I).

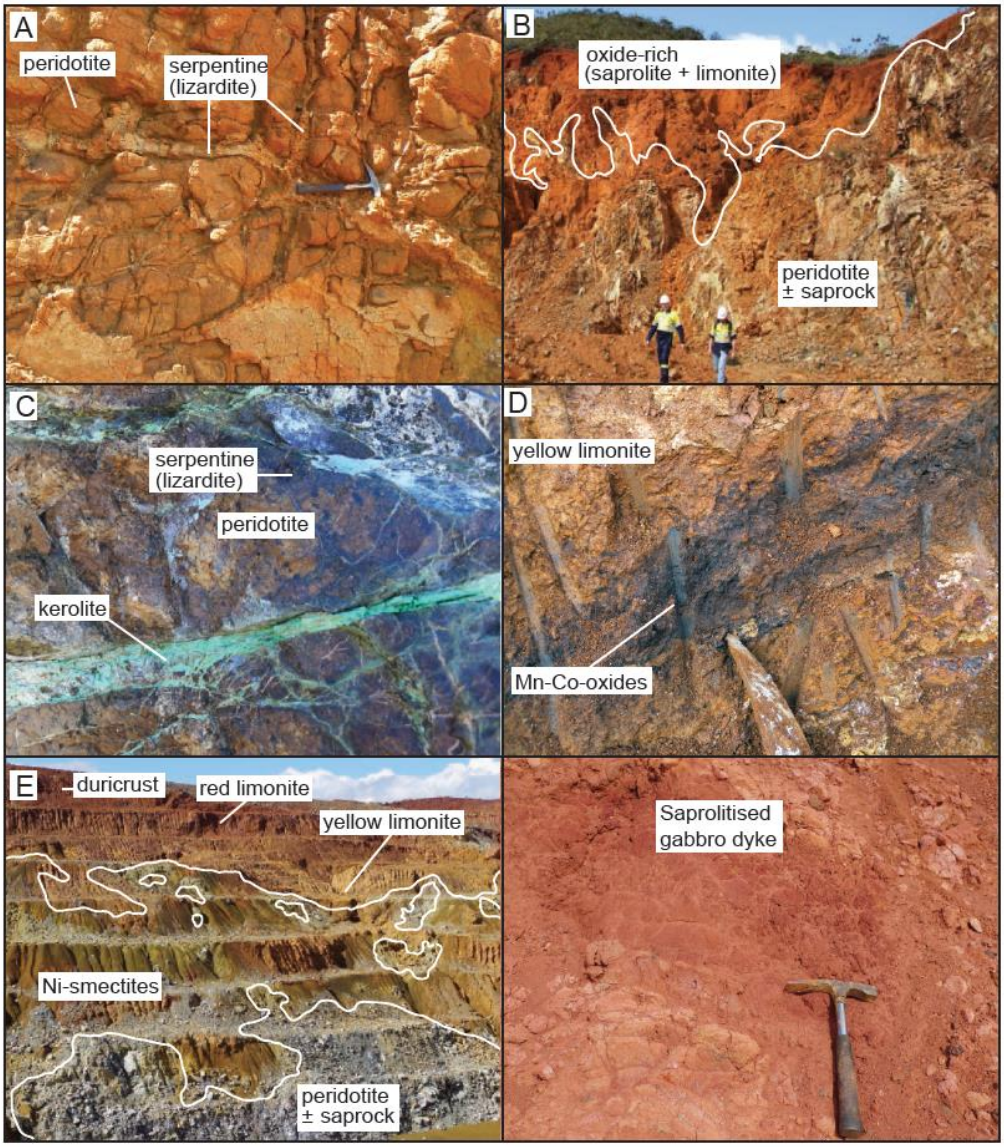

203

204 Fig. 3: Field photographs of representative lithofaciès as observed in the Koniambo, Cap Bocage and
205 Tiébaghi Ni-Co laterites. (A) Unweathered harzburgite with networks of serpentine (lizardite) veins
206 (Koniambo). (B) Typical sharp transition from silicate-dominated bedrock and saprock to oxide-
207 dominated saprolite and limonite (Koniambo). (C) Ni-rich talc-like (kerolite) vein developed at the
208 bedrock – saprock interface (Koniambo). (D) Mn-Co oxide-rich transition zone developed at the
209 saprolite – yellow limonite interface (Cap Bocage). (E) Well-developed Ni smectite-rich zone (up to >15
210 m in vertical thickness) above lherzolitic serpentinite at Tiébaghi. (F) gabbro saprolite with hematite
211 and kaolinite, cross-cutting limonitised lherzolite (Tiébaghi).

212

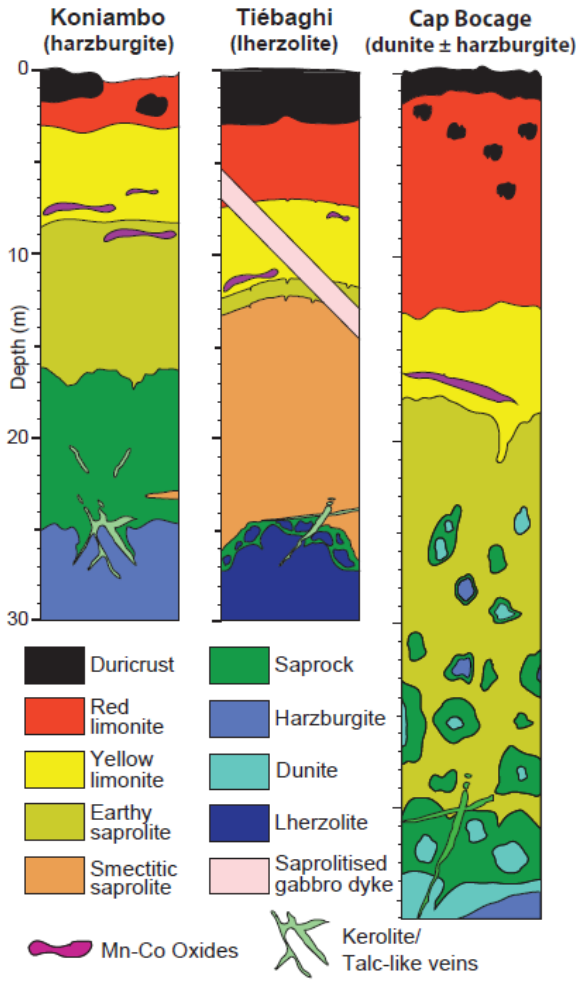

213

214 Fig. 4: Stratigraphic logs of representative Ni-Co laterites from the Koniambo, Cap Bocage and

215 Tiébaghi mines.

216

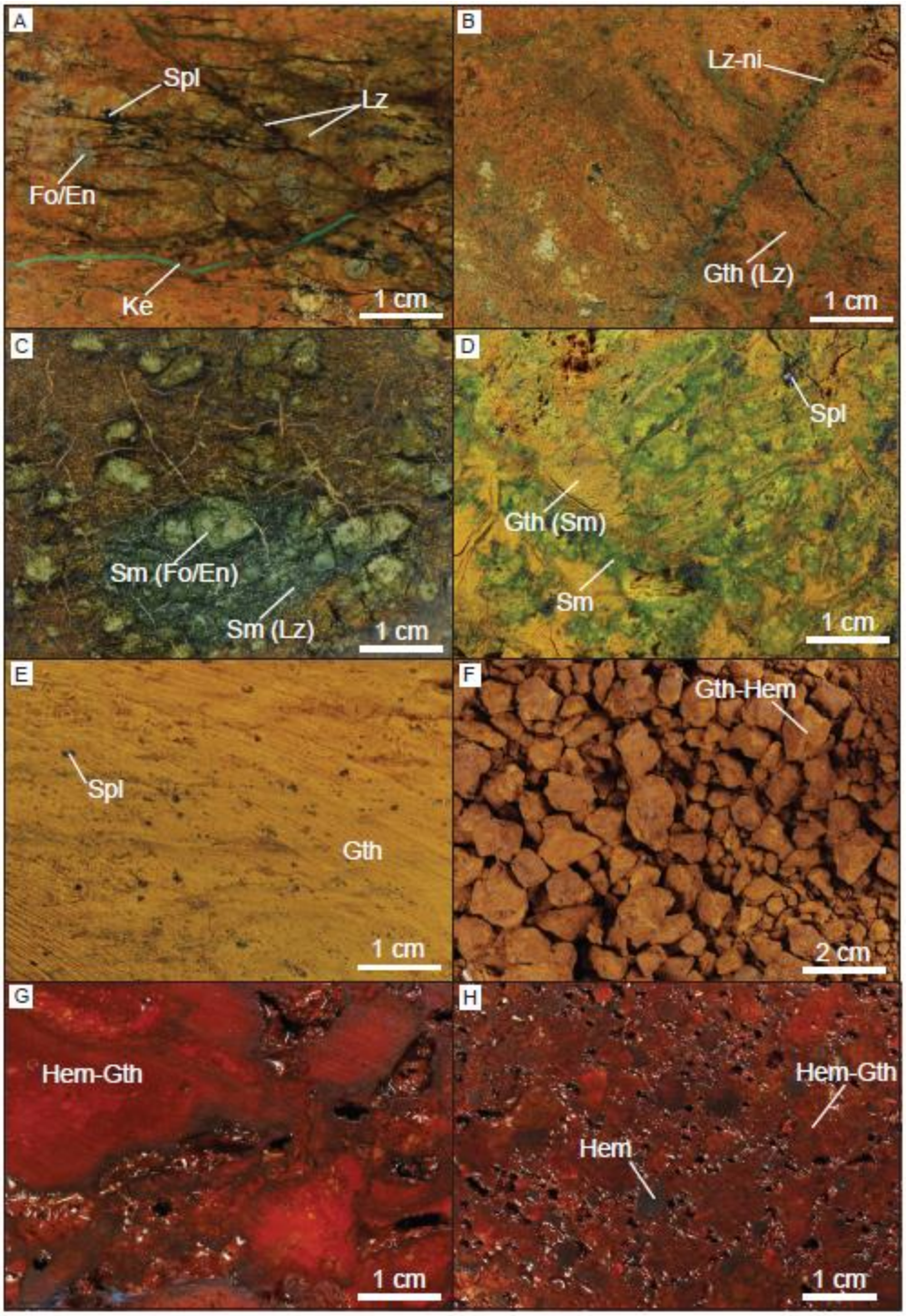

Fig. 5: Representative alteration facies observed in the investigated deposits. (A) Kerolite vein and slight goethitisation in the saprock developed after moderately serpentinised harzburgite (Koniambo). (B) Transition from saprock to earthy saprolite, marked by the disappearance of mantle silicate, Ni enrichment in the serpentine veins and the partial replacement of serpentine by goethite (Cap Bocage). (C) Complete replacement of lherzolite by smectite in the saprolite horizon (Tiébaghi), (D)

Transition from the smectitic saprolite to the yellow limonite (Tiébaghi). (E) Ochreous goethite-rich yellow limonite with residual enrichment in chromiferous spinel (Tiébaghi). (F) Pulverulent goethite-hematite-bearing red limonite (Cap Bocage). (G) Vesicular hematite-goethite-bearing lateritic residuum (Tiébaghi). (H) Nodular/pisolitic ferricrete (Tiébaghi). Mineral abbreviations: En = enstatite, Fo = forsterite, Gth = goethite, Hem = hematite, Ke = kerolite, Lz = lizardite, Lz-ni = nickel-enriched lizardite, Spl = chromiferous spinel. Precursor minerals are indicated in brackets.

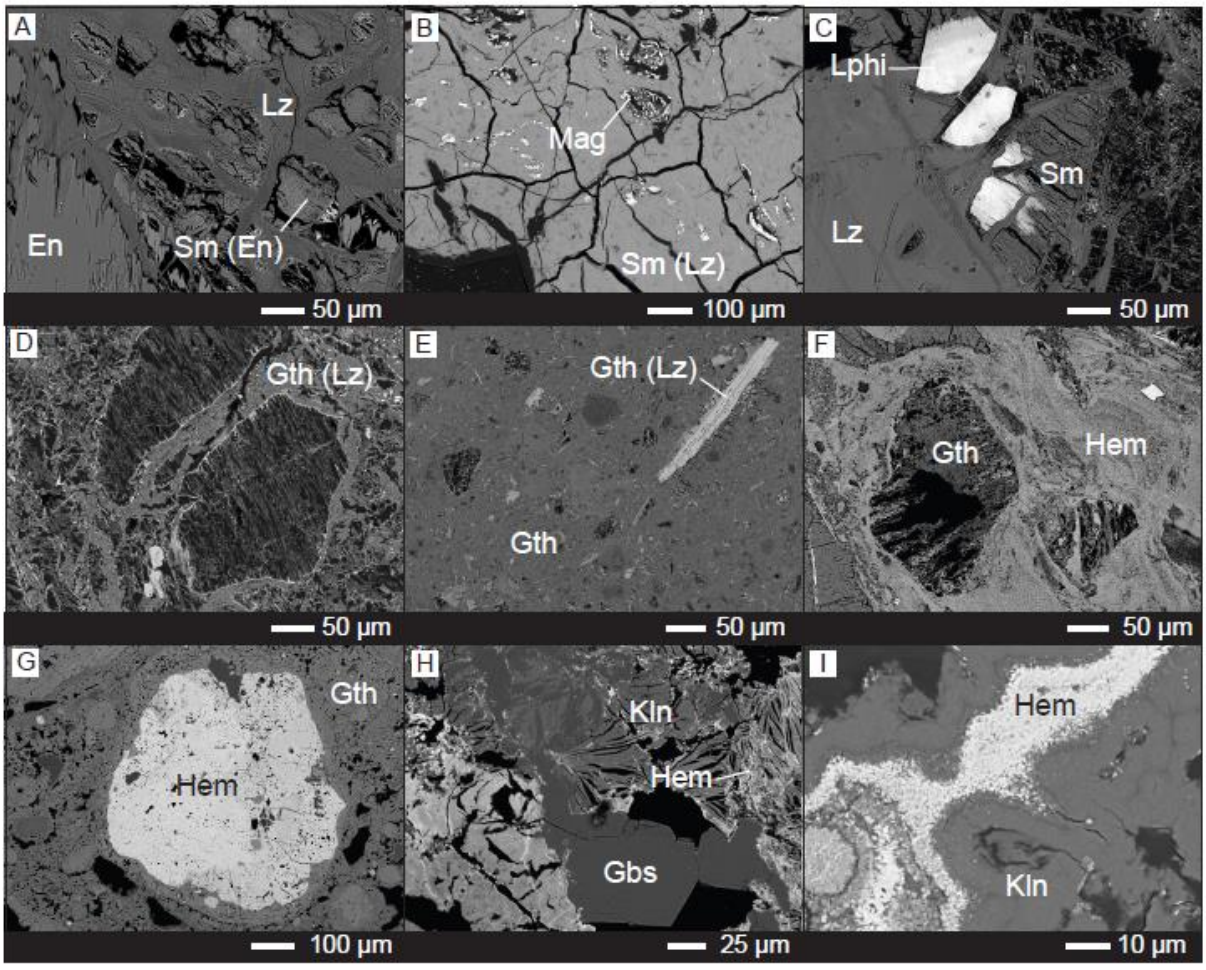

Fig. 6: Backscattered Electron (BSE) microphotographs. (A) Onset of mantle silicate dissolution (here enstatite) and partial epigenetic replacement by smectite at the bedrock-saprock interface (Koniambo). (B) Extensive replacement of lherzolite-dervied serpentinite by smectite in the saprolite (Tiébaghi). (C) Partial replacement of smectite by lithiophorite in the saprock/saprolite (Koniambo). (D) Epigenetic replacement of the serpentine vein mesh by ochreous goethite while preserving primary

textures in the earthy saprolite (Koniambo). (E) Advanced texture obliteration and fragmentation of pre-existing structures in the yellow limonite (Koniambo). (F) Recrystallisation of goethite and hematite with local preservation of inherited textures at the microscopic scale in the lateritic residuum, Tiébaghi. (G) Goethitic pisolitic cortexes overgrowing onto nodular hematite in a goethite-bearing cement, ferricrete horizon, Tiébaghi. Mineral abbreviations: Gbs = gibbsite, Kln = kaolinite, Lphi = lithiophorite, Mag = magnetite, Sm = smectite. See caption of Fig. 5 for additional abbreviations. Precursor minerals are indicated in brackets.

5. Whole-rock geochemical correlations at the deposit scale

Whole-rock geochemical analysis of the investigated lateritic profiles shows that the lateritisation of unweathered peridotites is associated with the progressive enrichment of poorly mobile elements. In particular, Fe, Al, Cr, and Sc concentrations co-increase during weathering, exhibiting positive correlation trends (Fig. 7, Supplementary Table 1). In the Ma-Oui deposit, Al_2O_3, Fe_2O_3, Cr_2O_3 and Sc concentrations progressively increase from the bedrock to the oxide-rich horizons up to about 6 wt%, 80 wt%, 4.5 wt% and 80 ppm, respectively. The Sc-Al_2O_3, Sc-Fe_2O_3 and Sc-Cr_2O_3 linear regression models encompassing variable lithofacies (unweathered harzburgite, saprock, saprolite, Mn-Co-rich transition zone, yellow and red limonite) provide a particularly relevant fit of the data (Fig. 7A). Scandium concentrations may be approximatively estimated from the Al_2O_3, Fe_2O_3 and Cr_2O_3 concentrations from the bedrock to the red limonite as follows:

(1) Sc (ppm) = 12.03* Al_2O_3 (wt%) + 2.42 ; R^2 = 0.93

(2) Sc (ppm) = 0.92* Fe_2O_3 (wt%) + 0.07 ; R^2 = 0.86

(3) Sc (ppm) = 16.27* Cr_2O_3 (wt%) + 0.31 ; R^2 = 0.91

The Sc-Fe_2O_3 correlation trend shows low dispersion in the low-Sc concentration range (0-50 ppm) but significant dispersion in the higher-Sc concentration range (50-80 ppm). In addition, two samples

collected in the transition and yellow limonite zone, respectively, fall well out of the Sc-Fe_2O_3 regression line. The Sc-Cr_2O_3 correlation trend is better defined, yet it presents moderate data dispersion. Comparatively, the best fit is obtained for the Sc-Al_2O_3 regression line, which exhibits the lowest dispersion of the data. Notably, the decrease in Al and Sc concentrations from the yellow to red limonite, as commonly identified by Teitler et al. (2019) in New Caledonian lateritic profiles, is not observed in the Ma-Oui geochemical dataset. In the Coquette Red tenement (Cap Bocage), Al_2O_3, Fe_2O_3, Cr_2O_3 and Sc concentrations increase to about 5 wt%, 80 wt%, 5.5 wt% and 65 ppm in the limonite, respectively. Like the Ma-Oui deposit, the Sc-Al_2O_3 regression line efficiently fits the data from the bedrock to the red limonite, although the laterite is developed on dunite and harzburgite (Fig. 7B). Analysed duricrust samples exhibit a large offset from the trend, with a substantial depletion in Sc relative to Al_2O_3. It is worth noting that the Sc-Al_2O_3 regression lines obtained at Ma-Oui and Coquette Red have similar regression coefficients (respectively 12.03 and 12.84; equations 1 and 4).

In contrast, Fe_2O_3, Cr_2O_3 and Sc concentrations do not correlate when considering the limonitic horizons. Therefore, Al_2O_3 here constitutes the only relevant explanatory variable for Sc concentrations among major elements. More specifically, Sc and Al_2O_3 are significantly enriched compared to Fe_2O_3 in the yellow limonite and, at the opposite, depleted in the red limonite. Regression lines obtained from Coquette Red samples, accounting for all lithologies apart from the duricrust, may be expressed as follows:

(4) Sc (ppm) = 12.84* Al_2O_3 (wt%) + 1.52 ; R^2 = 0.93

(5) Sc (ppm) = 0.68* Fe_2O_3 (wt%) + 3.91 ; R^2 = 0.82

(6) Sc (ppm) = 9.20* Cr_2O_3 (wt%) + 12.05 ; R^2 = 0.62

The East Alpha deposit (Fig. 7C), developed after strongly serpentinised lherzolite, exhibits Sc concentrations up to 115 ppm in the limonite, i.e. significantly higher than those observed at Ma-Oui and Coquette Red. Also, Al_2O_3 concentrations reach about 15 wt% in the lherzolite-derived limonite,

288 i.e. about three times more elevated than in the harzburgite±dunite-derived limonite at Koniambo and
289 Cap Bocage. In comparison, gabbro-derived saprolite yields Al_2O_3 concentrations up to about 30 wt%.
290 Maximum Fe_2O_3 and Cr_2O_3 concentrations at East Alpha are similar to those observed in the other
291 investigated sites, at 80 and 4 wt%, respectively. The Sc-Al_2O_3 regression line modelled for East Alpha
292 samples fits relatively well the data, except duricrust and gabbro samples that fall well out of the
293 correlation trend. The regression coefficient of the Sc-Al_2O_3 line is about twice lower at East Alpha than
294 at Ma-Oui and Coquette Red (equation 7). It is worth noting that smectitic saprolite samples from East
295 Alpha exhibit Al, Sc, Fe and Cr co-variations along a quite extensive concentration range (Fig. 7C).
296 Nevertheless, significant dispersion from the regression line is also observed in the yellow and red
297 limonite horizons compared to the Ma-Oui deposit and the Coquette Red tenement (Fig. 7C). Similar
298 to Coquette Red, Sc and Al_2O_3 are significantly enriched in the yellow limonite and depleted in the red
299 limonite compared to Fe_2O_3. The Sc-Fe_2O_3 and Sc-Cr_2O_3 correlations in the East Alpha deposit are
300 poorly defined, especially in the yellow and red limonite wherein Fe_2O_3, Cr_2O_3 and Sc concentrations
301 do not exhibit any correlation. Regression lines obtained for East Alpha, modelled after exclusion of
302 duricrust and gabbro-derived samples, may be expressed as follows:
303
304 (7) Sc (ppm) = 6.56* Al_2O_3 (wt%) + 7.55 ; R^2 = 0.83
305 (8) Sc (ppm) = 1.18* Fe_2O_3 (wt%) + 8.47 ; R^2 = 0.66
306 (9) Sc (ppm) = 24.08* Cr_2O_3 (wt%) + 9.48 ; R^2 = 0.62
307
308

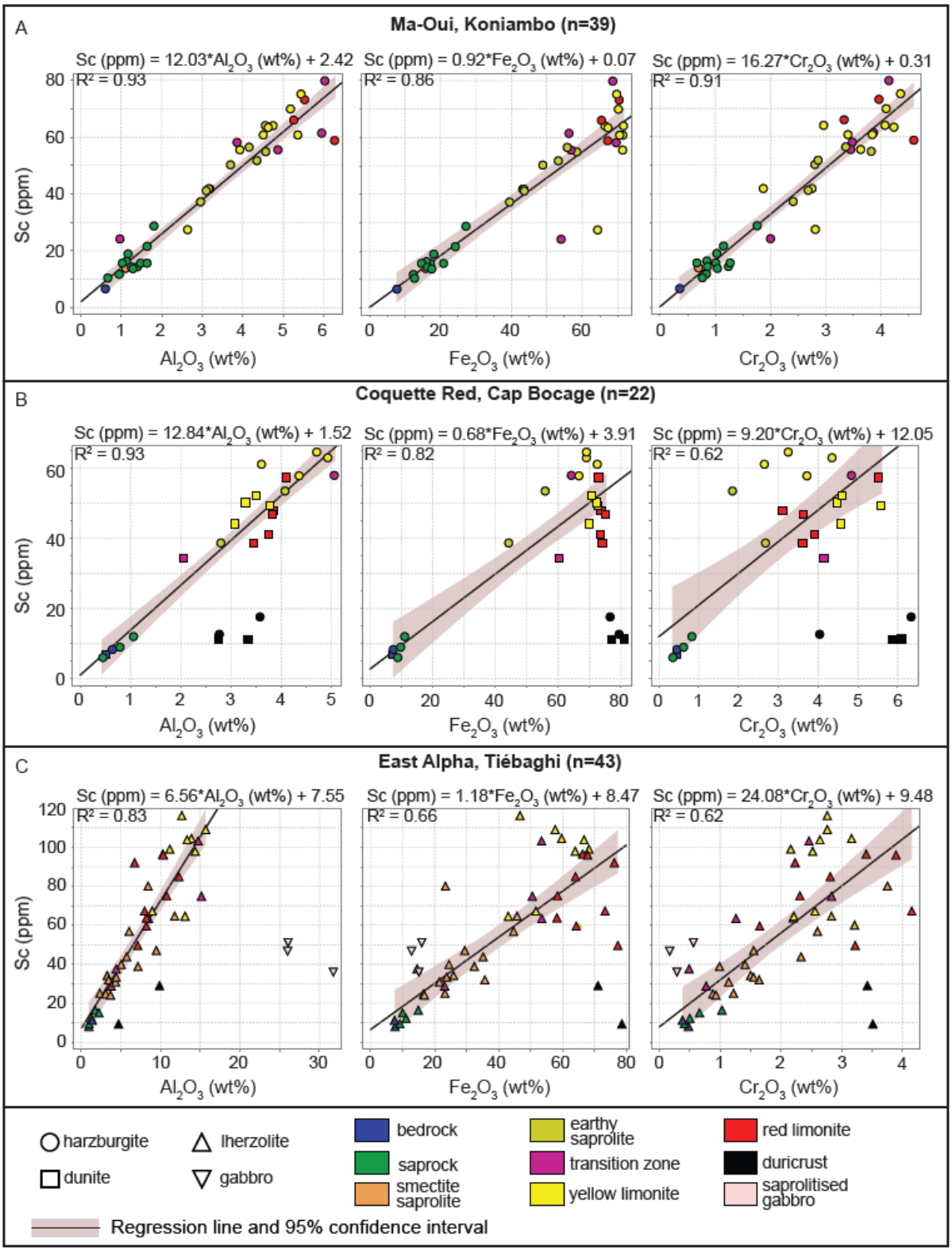

309

310 Fig. 7: Sc-Al_2O_3, Sc-Fe_2O_3 and Sc-Cr_2O_3 scatter plots and regression lines obtained for samples collected

311 at (A) the Ma-Oui deposit (Koniambo), (B) the Coquette Red tenement (Cap Bocage) and (C) the East

Alpha deposit (tiébaghi) (B). Peridotite-derived duricrust and gabbro-derived saprolite samples lie out of the correlation trends and are therefore excluded from the regression line modelling.

Principal Component Analysis (PCA) allows us to explore further the overall compositional variability of the samples and the strength of the colinearity between Sc and poorly mobile elements. The PCA, performed after centred log-ratio transformation of the data, shows that the cumulated explained variance in the PC1-PC2 plane reaches 78.4% of the overall variability of the initial dataset (respectively 53.0 and 25.4 % for PC1 and PC2, Fig. 8A, 8B). All of the elements constitutive of the samples except Mn and Co predominantly contribute to PC1, with Mg, Si and Ni having a positive contribution to PC1. At the same time, Fe, Al, Cr and Sc display a negative contribution to PC1 (Fig. 8B). PC1 therefore underlines a contrast between Mg-Si-Ni and Al-Sc-Fe-Cr, and PC2 describes the Mn and Co positive correlation. LOI exhibits a strong negative contribution to PC2. It is worth noting that the angles between Mg, Si and Ni rays are low, yet these rays are not coincident. Similarly, Sc and Al, on the one hand, and Fe and Cr, on the other hand, form two pairs of strongly coincident rays. These two pairs of coincident rays are at a relatively low angle, yet they are not colinear with one another. Sc is, therefore, better correlated with Al than with Fe or Cr. Regarding sample scores, bedrock samples fall close to the Mg ray. Saprock samples, in contrast, appear globally shifted towards the Si and Ni rays. Most smectitic saprolite samples still display a positive PC1 score, but lower than that of bedrock and saprock samples, with a low PC2 score. Earthy saprolite samples exhibit small positive and negative PC1 scores and significant shift towards positive PC2 scores. Earthy saprolite samples represent, therefore, intermediate compositions between the Mg-Si-Ni and the Al-Sc-Fe-Cr groups along PC1, together with the onset of an Mn-Co compositional signature along PC2. Comparatively, transition zone samples are slightly shifted towards negative PC1 scores, indicative of an increasing contribution of the Al-Sc-Fe-Cr group.

Moreover, transition zone samples exhibit the highest PC2 scores, consistent with their enrichment in Mn and Co. Yellow limonite samples are further shifted towards negative PC1 scores, while still displaying positive PC2 scores indicating the subsistence of an Mn-Co signature. Red limonite samples

also show negative PC1 scores but appear to be forming two subgroups, one with positive PC2 scores similar to the yellow limonite and one with negative PC2 scores, identical to duricrust samples.

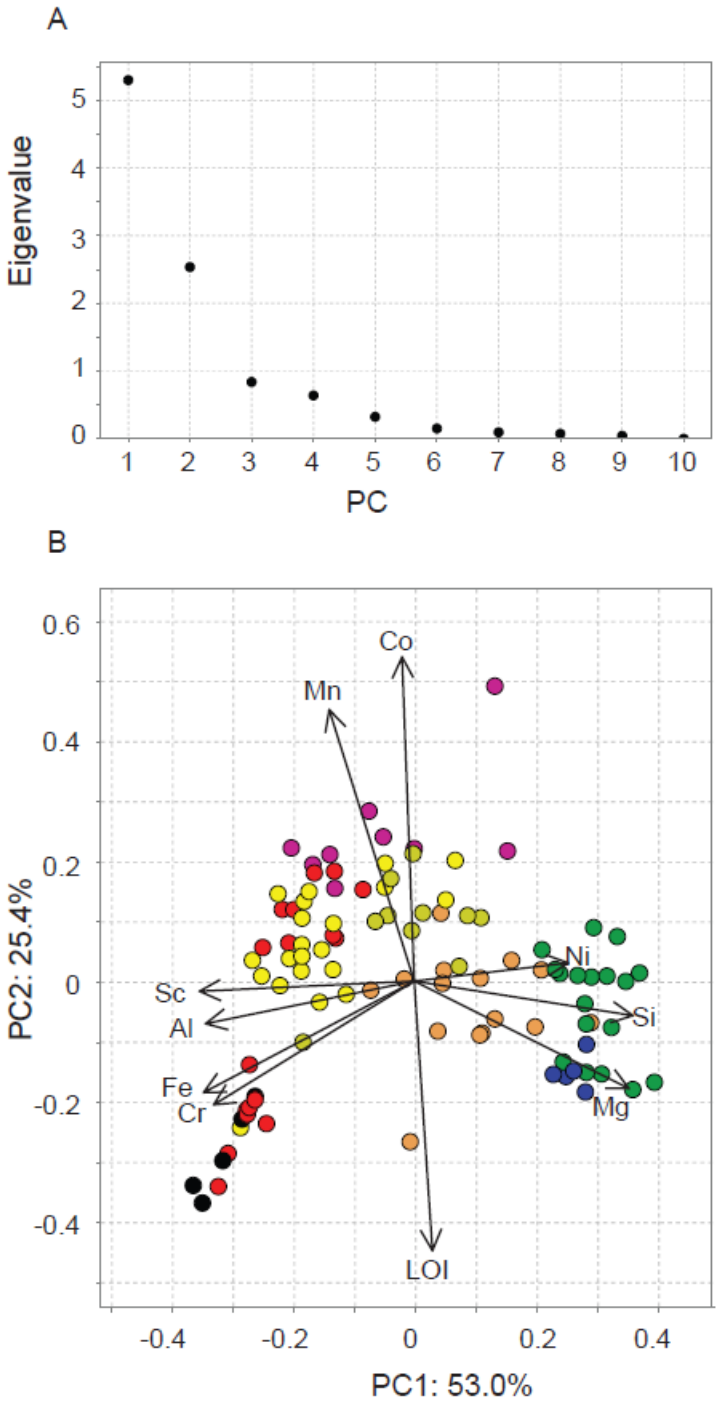

Fig. 8: Results of PCA performed after centred log-ratio transformation of Mg, Al, Si, Sc, Cr, Mn, Fe, Co, Ni concentrations and LOI from the global whole-rock geochemical dataset of peridotite-derived laterites (Ma-Oui, Coquette Red and East Alpha). Saprolitised gabbro samples from East Alpha were

345 excluded from PCA calculations. (A) Scree plot. (B) PC1-PC2 biplot showing variable loadings (arrays)
346 and sample scores (circles). See Fig. 7 for lithology colour coding.
347
348 **6. Mineral Chemistry**
349 The mineral chemistry data obtained from LA-ICP-MS analyses (Supplementary Table 2) allow us to
350 assess the contribution of primary mantle silicates to the Al and Sc budget in the unweathered
351 peridotites. Forsterite has a low Sc content in all of the investigated sites, about 3-6 ppm at Ma-Oui
352 and Coquette Red and about 7 ppm at East Alpha (Fig. 9), together with Al below detection limits.
353 Enstatite yields higher Sc and Al concentrations, which vary from one site to another. Sc concentrations
354 in enstatite from Ma-Oui and Coquette Red are similar (24 and 22.5 ppm, respectively). Al_2O_3
355 concentrations in enstatite are slightly higher at Ma-Oui (about 1.8 wt%) than at Coquette Red (about
356 1.4 wt%). In contrast, enstatite from East Alpha is enriched in Sc (about 32 ppm) and Al_2O_3 (about 3.4
357 to 3.8 wt%). Importantly, Sc-Al_2O_3 regression lines obtained from enstatite and forsterite mineral
358 compositions in each investigated site (Fig. 9) closely match those obtained from whole-rock
359 geochemical analysis throughout the weathering sequences (Fig. 7). More specifically, regression
360 coefficients estimated from mantle silicate mineral chemistry *versus* global whole-rock geochemistry,
361 respectively, are (i) 12.03 *vs* 11.02 at Ma-Oui, (ii) 13.18 *vs* 12.84 at Coquette Red, and (iii) 6.71 *vs* 6.56
362 at East Alpha.
363

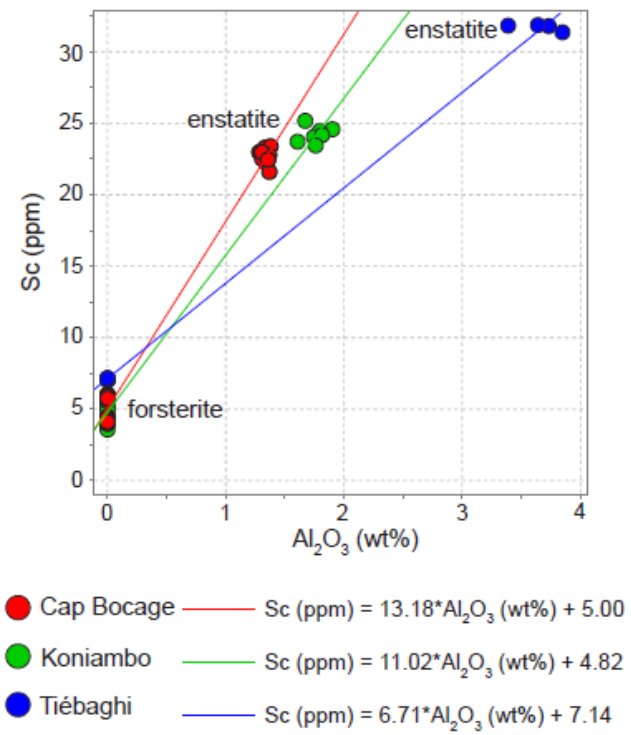

364

365 Fig. 9: Sc-Al_2O_3 scatterplot and regression lines obtained for mantle silicates (forsterite, enstatite) in
366 peridotite bedrocks from Ma-Oui (Koniambo), Coquette Red (Cap Bocage) and East Alpha (Tiébaghi)
367 from LA-ICP-MS analyses.

368

369 Further support for the intimate relationship between Sc-Al_2O_3 contents of peridotite mantle silicates
370 and Sc-Al_2O_3 contents of peridotite-derived laterite samples is provided by the mineral chemistry data
371 of secondary mineral phases along with laterite profiles as analysed at East Alpha (Fig. 10,
372 Supplementary Table 2). Together with forsterite and enstatite, Sc and Al_2O_3 concentrations in
373 smectite, ochreous goethite from the limonite zone, and goethite-hematite from the lateritic residuum
374 appear to be strongly proportional, with a regression line closely similar to that obtained from whole-
375 rock geochemistry. Smectite in the smectitic saprolite and ochreous goethite in the limonite exhibit
376 variable yet proportional Sc and Al_2O_3 concentrations. Indeed, Sc and Al_2O_3 concentrations in smectite
377 vary from 20 to 80 ppm and from 2.5 to 10 wt%, respectively, while Sc and Al_2O_3 concentrations in
378 limonitic, ochreous goethite vary from 55 to 122 ppm and from 7 to 16 wt%, respectively. Goethite-
379 hematite from the lateritic residuum is, comparatively, depleted both in Sc and Al_2O_3, yet it falls on or

close to the regression line. In contrast, goethite and hematite nodules and pisolitic cortexes from the ferricrete appear further depleted in Sc to fall below the regression line.

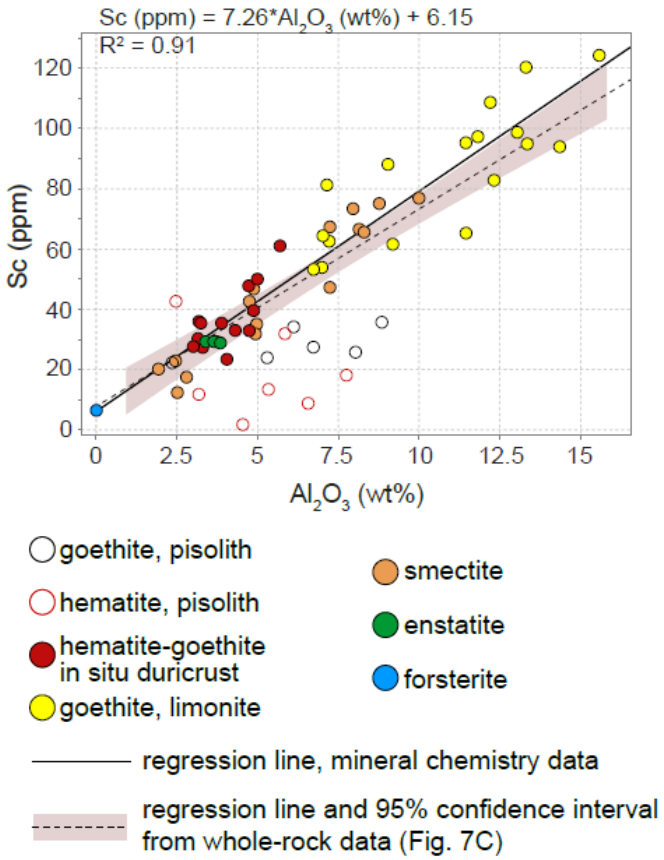

Figure 10: Sc-Al_2O_3 scatterplot and regression line obtained for silicates, smectite and iron oxides in the East Alpha deposit (Tiébaghi) from LA-ICP-MS analyses. The regression line calculation excluded spot analyses on goethite and hematite from the nodular/pisolitic duricrust.

7. Sequential extractions

The sequential extractions for Fe, Al, Ni and Sc are given in Fig. 11. The ultrapure water did not permit solubilising these elements in any investigated samples during the first extraction step. With regards to Fe, the hydroxylamine hydrochloride extraction also proved unsuccessful. In iron-rich samples (earthy saprolite, yellow and red limonite), about 10-15% of the total Fe mass was extracted during the subsequent extraction step involving ammonium oxalate, while about 50-60% was removed during the last extraction step involving citrate-bicarbonate-dithionite (CBD). In iron-rich lithologies, the

394 overall procedure therefore permits the extraction of 60 to 80% of the total Fe content, and CBD
395 appears the most effective reagent to solubilise Fe. In contrast, the general approach only resulted in
396 the extraction of about 25% of the total Fe in the smectitic saprolite sample (TIEA-08) from East Alpha,
397 mainly through the action of CBD and, to a lesser extent, of ammonium oxalate. With regards to Al,
398 the overall procedure succeeded in solubilising 40-50% and 10% of the total Al (Fig. 10A) in iron-rich
399 and smectite-rich samples, respectively. The relative amount of extracted Al is higher in iron-rich
400 samples from Coquette Red (PZ1B-06, PZ1B-09, PZ1B-13 and PZ1B-17) compared to their equivalents
401 from East Alpha (TIEA-07 and TIEA-12). Among this fraction, a small portion (less than 5% of the total
402 Al extracted) was solubilised using hydroxylamine hydrochloride. The relative amount of Al removed
403 by ammonium oxalate is similar to that of Fe, about 10% or less. CBD remains the most efficient reagent
404 for Al extraction but seems less effective for solubilising Al than Fe. In addition, Al appears more
405 efficiently extracted by ammonium oxalate in iron-rich samples from Coquette Red (about 10% of the
406 total Al or 15-30% of the whole extracted Al) than in their equivalent from East Alpha (about 5% of the
407 total Al or 10% of the extracted Al).
408 Bulk Ni extraction is similar or higher to Fe extraction. It is, in particular, higher in iron-rich samples
409 from Coquette Red than in their equivalents from East Alpha. More specifically, two samples from
410 Coquette Red (PZ1B-09 and PZ1B-17) show almost complete Ni extraction, while Ni extraction in East
411 Alpha does not exceed 60%. In contrast, Ni is weakly extracted from the smectitic saprolite sample
412 from East Alpha. The relative proportion of Ni removed by hydroxylamine hydrochloride remains low
413 (5 to 15% of the total Ni extracted) yet higher than that observed for Al. The efficiency of Ni extraction
414 by ammonium oxalate appears similar to that of Fe (about 5 to 15% of the total Ni extracted) and
415 slightly lower than Al. As for Fe and Al, Ni is best extracted through the last extraction step using CBD.
416 Regarding Sc, the extraction procedure proves efficient in oxide-rich samples, resulting in about 75%
417 of the total Sc amount, except in one sample (60% extraction efficiency in TIEA-07). Like Fe, neither
418 the ultrapure water nor the hydroxylamine hydrochloride extraction proved successful in extracting Sc

from any of the samples. Sc extraction using ammonium oxalate, which accounts for about 20 to 30% of the total Sc contained, appears significantly more efficient than Fe, Al and Ni in iron-rich samples. Nevertheless, in these samples, CBD remains the most efficient reagent for Sc extraction. In contrast, in the smectitic saprolite sample from East Alpha, Sc is almost exclusively extracted using ammonium oxalate. However, the total amount of extracted Sc from this sample remains moderate (about 50% of the bulk Sc content). To summarise, it should be noted that, in oxide-rich facies, (i) the extraction procedure is globally efficient for solubilising Fe, Al, Ni and Sc, though significant differences in global extraction efficiencies are observed depending on the considered element, and the sample provenance (ii) only Al and Ni can be slightly extracted using hydroxylamine hydrochloride, (iii) Fe, Al, Ni and Sc are best solubilised using CBD and, to a lesser extent, ammonium oxalate, (iii) the efficiency of Sc extraction using ammonium oxalate is significantly greater than that of Fe, Al and Ni. In contrast, the overall procedure is less well suited for the sequential extraction in smectitic saprolite, so the greater extraction efficiency of ammonium oxalate relative to other reagents must be considered cautiously.

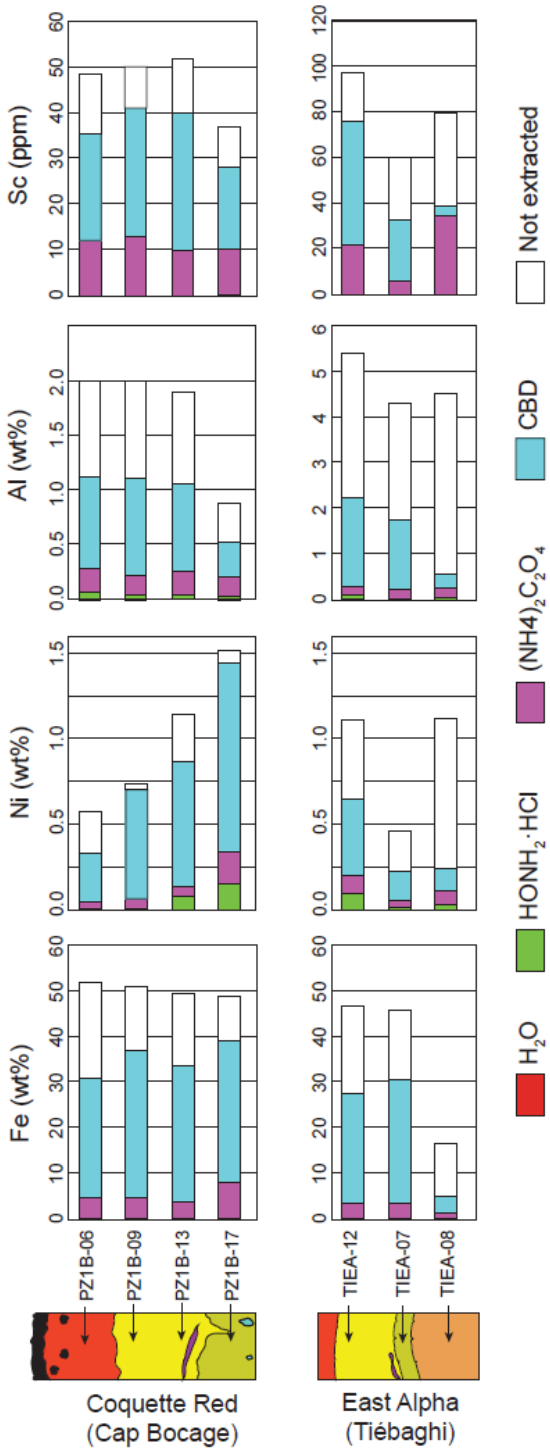

Figure 11: Results of sequential extractions. Cumulative histograms showing the total quantities of Fe (wt%), Ni (wt%), Al (wt%) and Sc (ppm) extracted with the different reagents, as well as the quantities not extracted. H_2O = Ultrapure water (step 1), $HONH_2$-HCl = hydroxylamine hydrochloride 0.1 mol.L-1 at pH 3.5 (step 2), $(NH4)_2C_2O_4$ = ammonium oxalate 0.2 mol.L-1 at pH 3 (step 3), CBD = citrate-

439 bicarbonate-dithionite $Na_2S_2O_4$ (22% Na-citrate and 1 g Na-dithionite) (step 4). See Fig. 7 for lithology
440 colour coding.
441
442 **8. Discussion and implications for the evaluation of Sc in Ni-Co laterites**
443 This study aims to assess in which conditions Al may be reliably used as a geochemical proxy for a first-
444 order evaluation of Sc grades and distribution in Ni-Co lateritic ores. In the following, we discuss the
445 causes of the Al-Sc co-variation regarding the mineralogical evolution in lateritic profiles and the
446 relevance of using deposit-scale Sc-Al_2O_3 correlations to assess the distribution of Sc in Ni-Co laterites.
447
448 ***8.1 Co-evolution of Al and Sc concentration and speciation through weathering***
449 Analytical data documented in the present contribution reveal significant correlations, at the deposit
450 scale, between Sc and Al_2O_3 concentrations in some lateritic Ni deposits of New Caledonia. The high
451 proportionality between Sc and Al_2O_3, observed in the investigated lateritic deposits from the bedrock
452 to the red limonite, is identified from whole-rock geochemistry (scatterplots of untransformed data
453 and PCA of centred log-ratio-transformed data) and mineral chemistry data (Fig. 7, 8, 10). Such
454 proportionality of whole-rock Sc and Al_2O_3 concentrations have already been documented by Teitler
455 et al. (2019), although the relevance of the Sc-Al_2O_3 correlation was not investigated at the deposit
456 scale. Also, the study conducted by Santoro et al. (2022) on trace element concentrations in goethite
457 from various Ni-laterite deposits showed a strong association between the Sc and Al contents of
458 goethite from the Wingellina deposit (Australia). The authors interpreted such association as being
459 primarily controlled by the composition of the parent rock, highlighting the influence of Al- and Sc-
460 bearing pyroxenite lenses on the composition of their goethite-bearing, weathered derivatives. The
461 Sc-Al_2O_3 proportionality, documented in the present contribution throughout the weathering
462 sequences of various Ni-laterites from New Caledonia (i.e. from the bedrock to the red limonite),
463 argues for a similar behaviour of Al and Sc during weathering.

464 In the unweathered mantle silicates, Ni is exclusively bound to forsterite. In contrast, virtually all of the
465 Al is hosted in pyroxenes (enstatite and diopside), and to a lesser extent, in chromiferous spinel, as it
466 is highly incompatible in forsterite. Sc is also predominantly hosted in pyroxenes, though forsterite
467 incorporates Sc up to a few ppm. Diopside contains significant concentrations of Sc (up to about 60
468 ppm; Teitler et al., 2019; Ulrich et al., 2019) but is not abundant (Table 1) and has a minor influence on
469 the bulk Sc content of unweathered lherzolite. Teitler et al. (2019) proposed that serpentinisation of
470 the peridotite most likely has a marginal effect on Sc concentrations in the bedrock. Therefore, the
471 global Sc and Al_2O_3 contents in unweathered peridotite mainly depend on the relative proportion of
472 enstatite and its chemical composition.
473 In the lower part of the weathering sequence (saprock and smectitic saprolite), Sc and Al
474 concentrations co-increase with Fe and Cr concentrations, suggesting that Sc and Al enrichments are
475 essentially residual. Co-variations, along a quite extensive concentration range, of Al, Sc, Fe and Cr in
476 smectitic saprolite samples from East Alpha (Fig. 7) result from inherent co-variation of smectite
477 composition, as evidenced by mineral chemistry data (Fig. 10). The sequential extraction procedure
478 proved relatively ineffective in solubilising Fe, Ni and Al and from the smectitic saprolite. These
479 elements are typically present in octahedral and tetrahedral positions in nickeliferous smectite (Mano
480 et al., 2014; Ratié et al., 2018) and are not leached easily from smectite. However, the significant
481 amounts of Sc extracted from the smectite-rich saprolite using ammonium oxalate raise questions
482 regarding the speciation of Sc in this horizon. Together with the elevated Sc concentrations measured
483 in smectite from LA-ICP-MS analysis, the lack of Fe extraction by ammonium oxalate rules out any
484 significant contribution of amorphous iron oxides/oxyhydroxides to the Sc budget in the smectite-rich
485 zone. Based on the scandium K-edge XANES analysis, Chassé et al. (2019) proposed that Sc in the
486 plasmic horizon of the Syerston-Flemington Sc laterite (Australia) is efficiently trapped in smectite
487 through incorporation into octahedral sites. Such interpretation seems unable to account for the high
488 quantities of Sc extracted using ammonium oxalate. Further investigations remain necessary to
489 evaluate the Sc speciation in the smectitic saprolite from the East Alpha deposit.

Contrasting with the Fe-Al-Sc-Cr collinearity identified in the lower portion of the weathering sequences, Sc and Al exhibit a relative enrichment compared to Fe in the earthy saprolite/yellow limonite and a relative depletion in the red limonite. This distribution pattern, observed at Coquette Red and East Alpha (Fig. 7B, 7C) as well as in several New Caledonian Ni-Co laterites (Teitler et al., 2019), but not at Ma-Oui (Fig. 7A), supports specific mobility of Sc and Al. It is suggested that these elements are, to some extent, remobilised from the red limonite and accumulated downwards in the yellow limonite. The remobilisation of Sc and Al possibly result from the release of Sc and Al after the dissolution/recrystallisation of increasingly crystallised goethite during the maturation of the lateritic profile (Dublet et al., 2015; Teitler et al., 2019). Such a model is commonly accepted for explaining the distribution pattern of Ni concentrations, which generally decrease gradually from the earthy saprolite upwards in conjunction with an increase of the mean coherent domain (MCD) size of the goethite crystallites (Dublet et al., 2012, 2015). This typical Ni distribution pattern is, for instance, well-evidenced at Coquette Red, where a gradual decrease of Ni concentrations occurs from the earthy saprolite (1.5 wt% Ni) to the red limonite (0.5 wt% Ni). There, Sc and Al distribute differently from Ni, as Sc and Al concentrations are higher in the yellow limonite than in the earthy saprolite. Although the release of Sc during dissolution/recrystallisation of goethite has been proposed as a relevant model for explaining some elevated Sc concentrations in the yellow limonite (Chassé et al., 2019; Teitler et al., 2019), the mobility of Sc released during this process must therefore be lower than that of Ni. In addition, the formation of hematite at the expense of goethite in the red limonite likely results in the downward redistribution of Sc and Al, as both Sc and Al substitute more easily for Fe in goethite than in hematite (Levard et al., 2018; Schwertmann and Latham, 1986; Trolard et al., 1995), thus contributing to Sc enrichment in the yellow limonite.

Sequential extraction provides further insights on the speciation of Sc and its association with other elements in the earthy saprolite, yellow and red limonite. It is worth noting that the extraction procedure here applied differs from the method used by Chassé et al. (2019) and Qin et al. (2020) on ultramafic-derived laterites from the Syerston-Flemington (Australia) and the Berong (Philippines)

516 deposits, respectively. In these two studies, the extraction procedure is adapted from Hall et al. (1996)
517 and Sanematsu et al. (2011). It includes sodium acetate as the first reagent to assess the adsorbed and
518 exchangeable species. In contrast, we used ultrapure water, which only allows us to extract the easily
519 exchangeable species and therefore does not estimate the adsorbed species.
520 Nevertheless, the extracted Sc amounts obtained by Chassé et al. (2019) and Qin et al. (2020) from
521 sodium acetate treatment are low (10-15%) in the Syerston-Flemington laterites to very low (<5%) in
522 the Borong laterites. These two studies combine sequential extraction with XANES analysis. Chassé et
523 al. (2019) observed that the low proportion of exchangeable goethite-hosted Sc obtained from
524 sequential extraction (10-15%) is at odds with the results of XANES analysis. The latter is interpreted
525 to reflect an elevated contribution of adsorbed Sc (up to 80%) in the global Sc budget of iron
526 oxides/oxyhydroxides and only a small proportion of Sc being substituted in iron oxides or
527 oxyhydroxides. The authors favour better reliability of the XANES spectra interpretation than the
528 sequential extraction results and propose reconciling these data by arguing for the high stability of the
529 Sc adsorption complex on goethite, thus preventing the extraction of adsorbed Sc through sodium
530 acetate treatment. Similarly, in the Gorong deposit (Qin et al., 2020), the amounts of Sc adsorbed on
531 goethite appear more significant when estimated from XANES spectra (24-49%) than from sequential
532 extraction (below 5%).
533 Both of these studies then use hydroxylamine hydrochloride to extract amorphous iron oxides. In
534 contrast, we used hydroxylamine hydrochloride at lower concentrations to extract manganiferous
535 species. No Fe nor Sc, and only a very slight fraction of Ni and Al, are extracted using hydroxylamine
536 hydrochloride, highlighting the marginal presence of Mn oxides in the investigated samples and the
537 absence of detectable Sc in Mn oxides. Following hydroxylamine hydrochloride treatment, we used
538 ammonium oxalate to extract amorphous iron oxides. Ammonium oxalate has been reported as an
539 efficient and selective dissolving agent for amorphous and poorly crystalline ferric
540 oxides/oxyhydroxides, without significant dissolution of crystalline goethite and hematite, nor
541 attacking silicates (Leermakers et al., 2019; Poulton and Canfield, 2005). Chassé et al. (2019) and Qin

et al. (2020) did not pursue sequential extraction further than the amorphous iron oxides/oxyhydroxides extraction step, hypothesizing that the residue is mostly representative of crystalline iron oxides. In the present study, the use of CBD as the last extraction step unambiguously demonstrates that crystalline iron oxides/oxyhydroxides predominates over amorphous iron oxides/oxyhydroxides in oxide-rich horizons. Along with Fe, the elevated Ni, Al and Sc fractions extracted using CBD confirm that these elements are mainly bound to crystalline goethite. At Coquette Red, a slight decrease in the proportion of total extracted Fe is observed from the earthy saprolite to the red limonite, from about 80 to 60% (Fig. 11). Such decrease, resulting from a slight lowering of both CBD and ammonium oxalate extraction efficiencies (from about 60 to 50% and 15 to 8%, respectively), may indicate the upwards increase in goethite crystallinity. Compared to Fe, Al extraction appears globally less effective, especially at East Alpha, wherein the Al contents of oxide-rich facies are higher than at Coquette Red. Such a discrepancy between the extraction efficiencies of Al and Fe possibly results from the presence of extraction-resistant, Al-bearing minerals in the oxide-rich facies. Chromiferous spinel, which is residually enriched in these horizons, contains about 15 wt% Al (Teitler et al., 2019). Therefore, even in minor amounts, the presence of extraction-resistant Cr-spinel implies that a non-negligible portion of the whole-rock Al content is hosted in Cr-spinel and cannot be extracted through the used procedure. However, such quantities of unextractable Al are likely insufficient to account for the apparent lower extractability of Al, nor for the differences in Al extraction rates between Coquette Red and East Alpha, as both sites have similar Cr contents. Alternatively, although not observed in any of the peridotite-derived limonite samples, the presence of trace amounts of kaolinite in the lherzolite-derived limonite cannot be ruled out at East Alpha. Similar to Cr-spinel, the used extraction procedure is ineffective in solubilising kaolinite, whose potential presence in the East Alpha limonite may explain the lower extraction rate for Al. Regarding Sc, total extraction rates in the Fe-rich horizons are similar to that of Fe (and therefore higher than that of Al), supporting the strong association of Sc with iron oxides/oxyhydroxides, and in particular with crystalline goethite. Nevertheless, ammonium oxalate appears relatively more efficient in extracting

568 Sc (about 20 to 35% of total Sc) than Fe (about 10% of the total Fe). The proportion of Sc extracted
569 from amorphous iron oxides in the present study is therefore slightly higher than that obtained by
570 Chassé et al. (2019), that is about 15-25%, and significantly higher than that obtained by Qin et al.
571 (2020), that is below 3%. This discrepancy possibly results from a better efficiency of ammonium
572 oxalate to extract Sc from amorphous iron oxides/oxyhydroxides than hydroxylamine hydrochloride.
573 Our results suggest that Sc may have a higher affinity for amorphous iron oxides/oxyhydroxides than
574 crystalline goethite. Significant amounts of Sc can be thus concentrated in amorphous iron
575 oxides/oxyhydroxides despite the predominance of crystalline goethite throughout the lateritic
576 sequence. The speciation of Sc in oxide-rich facies differs probably in part from that of Al. The latter is
577 mainly incorporated in the lattice of crystalline goethite and preserved in weathering-resistant Cr-
578 spinel. Yet, despite second-order differences between the speciation of Sc and Al_2O_3, these elements
579 show strong proportionality from the bedrock to the red limonite. As these elements (i) are both
580 mainly immobile during the weathering of peridotite, (ii) have a preferential affinity for goethite, and
581 (iii) are only moderately remobilised following recrystallisation and goethite replacement by hematite,
582 the composition of the parent rock remains the first-order control on their concentrations throughout
583 the weathering sequences. Thus, the Sc-Al_2O_3 regression lines obtained from forsterite-enstatite
584 mineral compositions are close to those obtained from weathering-related mineral compositions and
585 whole-rock geochemistry along weathering profiles. The slightly lower regression coefficients obtained
586 from whole-rock geochemistry than those obtained from mantle silicate mineral composition may
587 result from the second-order contribution of Cr-spinel to the global Al budget in whole-rock
588 geochemical compositions. These results indicate that (i) the Sc-Al_2O_3 content of enstatite in a given
589 peridotite bedrock drives the Sc-Al_2O_3 regression line within its weathered derivatives, and (ii) the
590 relative proportion of enstatite together with its Sc content primarily control the maximum Sc
591 concentrations reached in the yellow limonite.
592 Contrasting with the proportionality observed between Sc and Al_2O_3 from the bedrock up to the red
593 limonite, samples from the duricrust are out of the Sc-Al_2O_3 whole-rock correlation trends. Such offset,

previously documented by Teitler et al. (2019), possibly results from the contribution of allochthonous material to the duricrust. Indeed, in situ Sc analysis of goethite-hematite in duricrust, were identified as lateritic residuum, shows a good fit with the Sc-Al_2O_3 regression line obtained on saprolitic and limonitic minerals. On the opposite, nodular and pisolitic goethite and hematite from the ferricrete exhibit a relative depletion in Sc compared to Al, similar to the offsets identified in the whole-rock geochemical dataset. In the East Alpha deposit, the offset of gabbro-derived saprolite from the Sc-Al_2O_3 correlation trend also results from the allochthonous nature of the gabbro compared to the peridotite-derived Ni-Co laterite, together with the specific mineral assemblage of the gabbro-derived saprolite. The formation of kaolinite during the weathering of gabbro is related to its substantial Al content (Schwertmann et al., 2000; Teitler et al., 2019; Trolard and Tardy, 1989). As Sc is typically poorly concentrated into kaolinite (Chassé et al., 2017; Teitler et al., 2019; Ulrich et al., 2019), the weathering of gabbros may lead to Sc remobilisation and trapping into nearby yellow limonite, while Al remains concentrated in saprolitised gabbro as kaolinite. Consequently, Sc and Al_2O_3 may be positively correlated in lateritic deposits if kaolinite, or other Al-bearing phases such as gibbsite, are mostly absent from the lateritic profiles. The formation of kaolinite (or gibbsite) during the lateritisation process requires that the parent rock contains significant amounts of Al, so that Sc-Al_2O_3 correlation trends may only be observed in ultramafic-derived laterites, wherein the Al content is low.

7.2 Implications for the assessment of Sc in Ni-laterites

The relevance of using Al as a geochemical proxy to conduct a first-order estimation of Sc concentration and distribution in a given Ni-Co deposit depends both on the specific reliability of the Sc-Al_2O_3 correlation at the deposit scale and on the method used to characterise Al concentration and distribution. The reliability of the Sc-Al_2O_3 correlation may be influenced by (i) potential heterogeneities in the parent rock lithology, (ii) the occurrence of alteration facies containing Al-rich phases such as kaolinite or gibbsite and (iii) the inherent data dispersion in Sc-Al_2O_3 scatterplots. Interestingly, the alternance of harzburgite and dunite in the bedrock does not seem to significantly

affect the Sc-Al_2O_3 regression coefficient nor the dispersion of the data, providing that the composition of enstatite remains similar in both facies. Nevertheless, lithological heterogeneities involving a change in the composition of enstatite, elevated amounts of diopside and plagioclase (e.g. in some lherzolite facies), or the occurrence of mafic intrusive dykes, may cause significant variations of the Sc/Al_2O_3 concentration ratio both in the parent rocks and in their weathered derivatives. These potential variations of the parent rock lithology at the deposit scale may be tested by geological characterisation and geochemical assay data analysis. In addition, alteration facies containing significant amounts of Al-rich phases (e.g. kaolinite, gibbsite) are commonly characterised by a substantial deviation from the Sc-Al_2O_3 correlation trend, established from smectite- and Fe-oxide-dominated lithologies. The possible occurrence of Al-rich phases, typically poor in Sc, must be examined to prevent over-estimation of the Sc content. Al-rich phases are commonly associated with weathered intrusive rocks such as gabbros. Still, they may also form during the weathering of some peridotites that yield significant Al concentrations. In particular, some plagioclase-bearing lherzolites (not investigated in the present study) can exhibit Al_2O_3 contents up to ~4 wt% (Marchesi et al., 2009; Ulrich et al., 2010) and may consequently alter to kaolinite or gibbsite.

Geochemical homogeneity and low Al-content of the parent rock are, therefore, necessary conditions for the occurrence of a reliable Sc-Al_2O_3 correlation trend at the deposit scale. Determination of a reliable, deposit-scale Sc-Al_2O_3 correlation requires assessing the range of Al_2O_3 concentrations for which Sc is well correlated with Al_2O_3 through an adequate sampling strategy that encompasses the whole range of Al_2O_3 concentrations and the mineralogical diversity throughout the deposit. Finally, the inherent data dispersion in Sc-Al_2O_3 biplots may be variable depending on the investigated deposit. Therefore, the number of samples used for establishing the Sc-Al_2O_3 correlation must be adapted to the inherent data dispersion to develop a reliable correlation with a good correlation coefficient. Once verified, deposit-scale Sc-Al_2O_3 correlations may first prove useful to estimate Sc concentrations on surface outcrops or pit walls using portable devices such as pXRF. Indeed, the relatively low Sc concentrations observed in Ni-laterites (<100 ppm) limit the use of pXRF to directly assess Sc (Lacroix

et al., 2021) whereas Al concentrations, typically about a few wt%, can be confidently estimated using such a device. The slightly lower accuracy obtained on Al analysis from pXRF than from a classical assay analysis would only marginally affect the estimation of Sc. More importantly, applying this approach to deposits where Al is routinely assayed could provide a first-order Sc concentration and distribution estimate. The reliability of such estimation would depend on the reliability of the Sc-Al_2O_3 correlation and the reliability of the Al distribution model. Indeed, block models are developed firstly to estimate the resource and distribution of Ni both in saprolitic and limonitic facies. They rely on statistical variograms set explicitly for several metals (e.g. Si, Mg, Fe, Ni) but not necessarily Al. In such a case, a specific evaluation of the variability of Al in the limonitic facies may be beneficial.

Conclusion

This contribution examines the relevance of using Al as a geochemical proxy for first-order estimates of Sc distribution and concentration in some peridotite-hosted, Ni-Co laterites from New Caledonia. Apparent correlations are identified at the deposit scale between Sc and Al_2O_3 concentrations from the bedrock to the red limonite. These correlations put forward the similar behaviour of Al and Sc during the peridotite weathering, which concentrations are primarily issued from the residual enrichment. Local remobilisation from the uppermost horizons is shown. Al and Sc are both predominantly hosted in crystalline goethite, but Sc has a relatively higher affinity for amorphous iron oxides compared to Al. In all investigated deposits, the Sc-Al_2O_3 regression coefficient remarkably depends on the Sc content in enstatite. Providing that the parent lithology is homogeneous and relatively depleted in Al, reliable Sc-Al_2O_3 correlations may thus be determined at the deposit scale after analysing a limited number of spatially and chemically representative samples. An adequate sampling strategy is required to cover the range of Sc and Al_2O_3 concentrations throughout the deposit and to take in account potential occurrences of specific alteration facies that may affect the relevance of the deposit-scale correlation (ferricrete, weathered intrusive rocks, kaolinite- or gibbsite-bearing alterite). Although the zones of maximum Sc enrichment are situated above the zones of maximum Ni

and Co enrichment, Sc-rich limonite may overlap the Co-rich transition zone, so that the base of the limonite may yield elevated Co and Sc concentrations together with sub-economic Ni grades. In such conditions, lateritic ores may be valuably exploited for Ni, Co and Sc assuming cost-effective co-valorisation of these metals.

Acknowledgments

This work has been funded and logistically supported by the French National Research Agency through the national program "Investissements d'avenir" of the Labex Ressources 21 with the reference ANR-10-LABX-21-RESSOURCES21 and by the National Centre for Technological Research CNRT "Nickel et son environnement" based in Nouméa, New Caledonia (Project grants: 8PS2013-CNRT.CNRS/SCANDIUM and 9PS2017-CNRT.GEORESSOURCE/TRANSNUM). The authors would like to thank, Stephane Lesimple, Dr. Bernard Robineau and Olivier Monge from the Geological Survey of New Caledonia, together with France Bailly, Laurence Barriller and Fabien Trotet, from the National Centre for Technological Research, for their technical and logistical support as well as for sharing their extensive knowledge of the geology of New Caledonia. We are grateful to Société Le Nickel (SLN), and Koniambo Nickel SAS (KNS), and in particular to Clément Marcaillou, Matthieu Monnerais, Hubert Dumon and Ludovic Levy, for support and access to mines and drill cores. We also thank Dr. Christophe Cloquet (SARM analytical centre, CRPG, Vandœuvre-lès-Nancy, France), Dr Andreï Leconte (GeoRessources, Vandœuvre-lès-Nancy, France) and Claude Douchement (NiLab laboratory, Pouembout, New Caledonia) for technical support in providing analytical data.

References

Aiglsperger, T., Proenza, J.A., Lewis, J.F., Labrador, M., Svojtka, Rojas-Puron, A., Longo, F., Durisova, J. 2016. Critical metals (REE, Sc, PGE) in Ni laterites from Cuba and the Dominican Republic. Ore Geology Reviews 76 (1) 127-147.

698 Anand, R. R., Smith, R. E., Paine, M. D. 2002. Genesis, classification and atlas of ferruginous materials,
699 Yilgarn Craton. Australian Mineral Industries Research Association. CRC LEME (Australia).
700
701 Audet, M. 2008. Le massif du Koniambo, Nouvelle-Calédonie. Formation et obduction d'un complexe
702 ophiolitique du type SSZ. Enrichissement en nickel, cobalt et scandium dans les profils résiduels. Ph.D
703 thesis, université de la Nouvelle Calédonie / Université du Quebec à Montréal, 326 pp.
704
705 Bailly, L., Ambrosi, J.P., Barbarand, J., Beauvais, A., Cluzel, D., Lerouge, C., Prognon, C., Quesnel, F.,
706 Ramanaïdou, E., Ricordel-Prognon, C., Ruffet, G., Sevin, B., Wells, L., Yans, J. 2014. Projet NICKAL:
707 "Typologie des minerais latéritiques de Nouvelle-Calédonie et facteurs de concentration de Co et Ni",
708 rapport final, BRGM/RP-63 482-FR, 402 pp.
709
710 Butt C.R.M., Cluzel D. 2013. Nickel laterite ore deposits: weathered serpentinites. Elements 9.123-128.
711
712 Cathelineau, M., Quesnel, B., Gautier, P., Boulvais, P., Couteau, C., Drouillet, M. 2016. Nickel dispersion
713 and enrichment at the bottom of the regolith: formation of pimelite target-like ores in rock block joints
714 (Koniambo Ni deposit, New Caledonia). Mineralium Deposita 51 (2), 271-282.
715
716 Cathelineau, M., Myagkiy, A., Quesnel, B., Boiron, M.-C., Gautier, P., Boulvais, P., Ulrich, M., Truche, L.,
717 Golfier, F., Drouillet, M. 2017. Multistage crack seal vein and hydrothermal Ni enrichment in
718 serpentinized ultramafic rocks (Koniambo massif, New Caledonia). Mineralium Deposita 52 (7), 945-
719 960.
720
721 Chassé, M., Griffin, W.L., O'Reilly, S.Y., Calas, G. 2017. Scandium speciation in a world-class lateritic
722 deposit. Geochemical Perspectives Letters 3, 105–114.
723

724 Chassé, M., Griffin, W.L., O'Reilly, S.Y., Calas, G. 2019. Australian laterites reveal mechanisms governing
725 scandium dynamics in the critical zone. Geochimica et Cosmochimica Acta 260, 292-310.
726
727 Cluzel, D., Aitchison, J.C., Picard, C. 2001. Tectonic accretion and underplating of mafic terranes in the
728 Late Eocene intraoceanic fore-arc of New Caledonia (Southwest Pacific): geodynamic implications.
729 Tectonophysics 340 (1-2), 23-59.
730
731 Cluzel, D., Maurizot, P., Collot, J., Sevin, B. 2012. An outline of the Geology of New Caledonia; from
732 Permian–Mesozoic Southeast Gondwanaland active margin to Cenozoic obduction and supergene
733 evolution. Episodes 35 (1), 72-86.
734
735 Dublet, G., Juillot, F., Morin, G., Fritsch, EM; Fandeur, D., Ona-Nguema, G., Brown Jr., G.E. 2012. Ni
736 speciation in a New Caledonian lateritic regolith: A quantitative X-ray absorption spectroscopy
737 investigation. Geochimica et Cosmochimica Acta 95, 119–133.
738
739 Dublet, G., Julliot, F., Morin, G., Fritsch, E., Fandeur, D., Brown Jr., G.E. 2015. Goethite aging explains
740 Ni depletion in upper units of ultramafic lateritic ores from New Caledonia. Geochimica et
741 Cosmochimica Acta 160, 1–15.
742
743 Dublet, G., Julliot, F., Brest., J., Noël, V., Fritsch, E., Proux, O., Olivi, L., Ploquin, F., Morin, G. 2017.
744 Vertical changes of the Co and Mn speciation along a lateritic regolith developed on peridotites (New
745 Caledonia). Geochimica et Cosmochimica Acta 217, 1–15.
746
747 Freyssinet, P.H., Butt, C.R.M., Morris, R.C., Piantone, P. 2005. Ore-Forming Processes Related to
748 Lateritic Weathering. In: Hedenquist JW, Thomson JFH, Goldfarb RJ, Richards JP (eds), Economic

749 Geology 100th Anniversary Volume. Economic Geology Publishing Company, New Haven, Connecticut,
750 pp. 681-722.
751
752 Golightly, J.P. 2010. Progress in understanding the evolution of nickel laterites. In: Goldfarb RJ, Marsh
753 EE, Monecke T (eds) The Challenge of Finding New Mineral Resources: Global Metallogeny, Innovative
754 Exploration, and New Discoveries Volume II. Society of Economic Geologists Special Publication 15, pp.
755 451-475.
756
757 Hall, G.E.M., Vaive, J.E., Beer, R., Hoashi, M. 1996. Selective leaches revisited, with emphasis on the
758 amorphous Fe oxyhydroxide phase extraction. Journal of Geochemical Exploration 56, 79-78.
759
760 Hoatson, D.M., Jaireth, S., Miezitis, Y. 2011. The major rare-earth-element deposits of Australia:
761 geological setting, exploration, and resources. Geoscience Australia, 204 pp.
762
763 Lacroix, E. Cauzid, J., Teitler, Y. Cathelineau, M. 2021. Near real-time management of spectral
764 interferences with portable X-ray fluorescence spectrometers: application to Sc quantification in
765 nickeliferous laterite ores. Geochemistry: Exploration, Environment, Analysis 21, 1-13.
766 https://doi.org/10.1144/geochem2021-015
767
768 Leermakers, M., Mbachou, B.E., Husson, A., Lagneau, V., Descostes, M. 2019. An alternative sequential
769 extraction scheme for the determination of trace elements in ferrihydrite rich sediments. Talanta 199,
770 80-88.
771
772 Levard, C., Borschneck, D., Grauby, O., Rose, J., Ambrosi, J.P. 2018. Goethite, a tailor-made host for the
773 critical metal scandium: The $Fe_xSc_{(1-x)}OOH$ solid solution. Geochemical Perspectives Letters 9, 16–20.
774

775 Manceau, A., Schlegel, M.L., Musso, M., Sole, V.A., Gauthier, C., Petit, P.E., Trolard, F. 2000. Crystal
776 chemistry of trace elements in natural and synthetic goethite. Geochimica et Cosmochimica Acta 64
777 (21), 3643–3661.
778
779 Mano, E.S., Caner, L., Petit, S., Chaves, A.P., Mexias, A.S. 2014. Mineralogical characterization of Ni-
780 bearing smectites from Niquelandia, Brazil. Clays and Clay Minerals, 62 (4), 324-335.
781
782 Marchesi, C., Garrido, C.J., Godard, M., Belleyd, F., Ferré, E. 2009. Migration and accumulation of ultra-
783 depleted subduction-related melts in the Massif du Sud ophiolite (New Caledonia). Chemical Geology
784 266 (3-4), 171-186.
785
786 Maulana, A., Sanematmatmatsu, K., Sakakibara, M. 2016. An Overview on the Possibility of Scandium
787 and REE Occurrence in Sulawesi, Indonesia. Indonesian Journal of Geoscience 3, 139–147.
788
789 Maurizot, P., Vendé-Leclerc, M. 2009. New Caledonia geological map, scale 1/500 000, Direction de
790 l'Industrie, des Mines et de l'Énergie – Service de la Géologie de Nouvelle-Calédonie, Bureau de
791 Recherches Géologiques et Minières.
792
793 Maurizot, P., Sevin, B., Lesimple, S., Bailly, L., Isepp,i M., Robineau, B. 2020. Mineral resources,
794 prospectivity of the ultramafic rocks of New Caledonia. Geological Society, London, Memoirs, 51, 247–
795 277. https://doi.org/10.1144/M51-2016-17.
796
797 Paquette, J.L., Cluzel, D. 2007. U–Pb zircon dating of post-obduction volcanic-arc granitoids and a
798 granulite-facies xenolith from New Caledonia. Inference on Southwest Pacific geodynamic models.
799 International Journal of Earth Sciences 96 (4), 613-622.
800

801 Poulton, S.W., Canfield, D.E. 2005. Development of a sequential extraction procedure for iron:
802 implications for iron partitioning in continentally derived particulates, Chem. Geol. 214 (3–4), 209–221.
803
804 Qin, H.-B., Yang, S., Tanaka, M., Sanematsi, K., Arcilla, C., Takahashi, Y. 2020. Chemical speciation of
805 scandium and yttrium in laterites: New insights into the control of their partitioning behaviors.
806 Chemical Geology 552, 1-15.
807
808 Ratié, G., Garnier, J., Calmels, D., Vantelon, D., Giumaraes, E., Monvoisin, G., Nouet, J., Ponzevera, E.,
809 Quantin, C. 2018. Nickel distribution and isotopic fractionation in a Brazilian lateritic regolith: Coupling
810 Ni isotopes and Ni K-edge XANES. Geochimica et Cosmochimica Acta 230, 137-154.
811
812 Royset, J., Ryum, N. 2005. Scandium in aluminium alloys, International Materials Reviews 50 (1), 19-
813 44.
814
815 Sanematsu, K., Moriyama, T., Sotouky, L., Watanabe, Y. 2011. Mobility of Rare Earth Elements in Basalt-
816 Derived Laterite at the Bolaven Plateau, Southern Laos. Resource Geology 61 (2), 140-158.
817
818 Santoro, L., Putzolu, F., Mondillo, N., Boni, M., herrington, R. 2022. Trace element geochemistry of
819 iron-(oxy)-hydroxides in Ni(Co)-laterites: Review, new data and implications for ore forming processes.
820 Ore Geology Reviews 140. https://doi.org/10.1016/j.oregeorev.2021.104501.
821
822 Schwertmann, U., Latham, M. 1986. Properties of iron oxides in some New Caledonian oxisols.
823 Geoderma 39, 105-123.
824

825 Schwertmann, U., Friedl, J., Stanjek, H., Schulze, D.G. 2000. The effect of Al on Fe oxides. XIX. Formation
826 of Al-substituted hematite from ferrihydrite at 25°C and pH 4 to 7. Clays and Clay Minerals 48 (2), 159-
827 172.
828
829 Sun, J., Liu, Y., Liu, X. 2021. Iron isotope constraints on the mineralization process of Shazi Sc-rich
830 laterite deposit in Qinglong county, China. Minerals 11, 737. https://doi.org/10.3390/min11070737.
831
832 Teitler, Y., Cathelineau, M., Ulrich, M., Ambrosi, J.P., Muñoz, M., Sevin, B. 2019. Petrology and
833 geochemistry of scandium in New Caledonian Ni-Co laterites. Journal of Geochemical exploration 196
834 131-155.
835
836 Toropova, L.S., Eskin, D.G., Kharakterova, M.L., Dobatkina, T.V. 1998. Advanced Aluminium Alloys
837 Containing Scandium. Structure and Properties, Gordon and Breach Science Publishers, Amsterdam,
838 pp. 175.
839
840 Trescases, J.-J. 1975. L'evolution Géochimique Supergène des Roches Ultrabasiques en Zone Tropicale:
841 Formation des Gisements Nickélifères de Nouvelle-Calédonie Edited, Paris, O.R.S.T.O.M., France.
842
843 Trolard, F., Tardy, Y. 1989. A model of Fe^{3+}-kaolinite-Al^{3+}-goethite-Al^{3+}-hematite equilibria in laterites.
844 Clay Minerals 24, 1-21.
845
846 Trolard, F., Bourrie, G., Jeanroy, E., Herbillon, A.J., Martin, H. 1995. Trace metals in natural iron oxides
847 from laterites: A study using selective kinetic extraction. Geochimica et Cosmochimica Acta 59 (7),
848 1285-1297.
849

Ulrich, M., Picard, C., Guillot, S., Chauvel, C., Cluzel, D., Meffre, S. 2010. Multiple melting stages and refertilization as indicators for ridge to subduction formation: The New Caledonia ophiolite. Lithos 115, 223-236.

Ulrich, M., Cathelineau, M., Muñoz, M., Boiron, M.C., Teitler, Y., Karpoff, A.M. 2019. The relative distribution of critical (Sc, REE) and transition metals (Ni, Co, Cr, V) in some Ni-laterite deposits of New Caledonia. Journal of Geochemical exploration 197, 93-113.

U.S. Geological Survey. 2022. Scandium. In: Mineral Commodity Summaries. U.S. Geological Survey, Reston, USA, 146–147

Wells, M.A., Ramanaidou, E.R., Verrall, M., Tessarolo, C. 2009. Mineralogy and crystal chemistry of "garnierites" in the Goro lateritic nickel deposit, New Caledonia. European Journal of Mineralogy 21 (2), 467-483.

Appendix A

Whole-rock geochemistry

Batch 1 sample pulps were analysed for whole-rock major- and trace-element geochemistry using the procedure of Carignan et al. (2001). Major element oxides and Sc were analysed using an iCap6500 ICP-OES with Li borate fusion. Trace elements were analysed using an iCapQ ICP-MS with Li borate fusion followed by nitric acid digestion. Analytical accuracy (2s standard deviation) lies within the typical uncertainty of the analytical data for both major element oxides and trace elements, which is less than 1% for major oxides and less than 5% for most trace elements. Batch 2 samples were analysed for major elements, Ni, Co and Sc, using an Axios FAST Wavelength Dispersive XRF spectrometer with LiF200 crystal. The detection limit for Sc is 12 ppm, and analytical accuracy is less than 7% in the 50-

120 ppm concentration range. The relative analytical precision between the two datasets, tested by duplicating the analysis of 3 samples in both laboratories, is better than 2% for Sc.

LA-ICP-MS

LA-ICP-MS analysis of Sc in silicates and phyllosilicates was performed with the NIST60 reference standard using Si concentration obtained from EMPA as internal standard. For oxides, analysis was performed with the StdGoe 1.1 pelletised goethite standard developed and validated by Ulrich et al. (2019) and using Fe concentration as an internal standard. Reference standards were analysed before and after every 15 ablations conducted on samples. Before each analysis, the background signal, or gas blank, was measured for a duration of 25 s. Ablation time, spot sizes and laser pulse frequency were 45 s, 60 µm, and 5 Hz, respectively. Data processing was conducted using the SILLS program (Guillong et al., 2008). The detection limit was below 1 ppm for most trace elements.

PCA on CLR-transformed geochemical data

Principal Component Analysis (PCA) was conducted on whole-rock geochemical data using the atomic weight percentages of Mg, Al, Si, Sc, Cr, Mn, Fe, Co, Ni and LOI following centred log-ratio (CLR) transformation to avoid spurious proportionality and boundary effects (Aitchison, 1986; Tolosana-Delgado & McKinley, 2016). PCA consists in transforming a multivariate dataset - here, each elemental concentration represents a variable - into a lower-dimensional dataset while preserving as much of the data's variation as possible. The dataset is projected into a new coordinate system based on the principal components, which are orthogonal linear combinations of original variables and corresponding to the eigenvectors of the covariance matrix. The advantage of such analysis is that principal components are likely controlled by mineral stoichiometry, providing a more realistic representation of geological variability. Centred log-ratio transformation of Mg, Al, Si, Sc, Cr, Mn, Fe, Co, Ni concentrations and LOI performed before PCA has the benefit of removing the proportionality effect (i.e. the predominance of major elements on the geochemical variability) and the boundary

effects (negative bias and spurious correlation effect; Chayes, 1960). Saprolitised gabbro samples from East Alpha were excluded from PCA calculations to explore better the impact of weathering on peridotite bedrocks alone. In a covariance biplot of log-ratio transformed data, a short distance between the ray tips of two variables (i.e. coincident rays) indicates that these variables are highly proportional (Tolosana-Delgado & McKinley, 2016).

Sequential extractions

Sequential extractions were conducted on seven Sc-bearing samples from Cap Bocage and Tiébaghi, encompassing earthy saprolite, smectitic saprolite, yellow and red limonite facies. For each extraction, approximately 1 g of sample powder (<50 µm) was weighed into 50 mL of reagent solution and agitated for 76 h. Each tube was then centrifugated at 10000 rpm, and the supernatant liquid was filtered at 0.2 µm before ICP-AES analysis. The residue was then rinsed with Milli-Q® water and used for subsequent extraction after re-suspension.

Appendix A references

Chayes, F. 1960. On correlation between variables of constant sum. J. Geophys. Res. 65 (12), 4185-4193

Aitchison, J. 1986. The Statistical Analysis of Compositional Data. Monographs on Statistics and Applied Probability. Chapman & Hall Ltd., London (UK) (Reprinted in 2003 with additional material by The Blackburn Press).

Carignan, J., Hild, P., Mevelle, G., Morel, J., Yeghicheyan, D. 2001. Routine Analyses of Trace Elements in Geological Samples using Flow Injection and Low Pressure On-Line Liquid Chromatography Coupled

927 to ICP-MS: A Study of Geochemical Reference Materials BR, DR-N, UB-N, AN-G and GH. Geostandards
928 and Geoanalytical Research 25 (2-3), 187-198.
929
930 Guillong, M.M., Maier, D.L., Allan, M.M., Heinrich, C.A. 2008. SILLS: a MATLAB based program for the
931 reduction of laser ablation ICPMS data of homogeneous materials and inclusions. In: Sylvester, P. (Ed.),
932 Laser Ablation ICPMS in the Earth Sciences. Current Practices and Outstanding Issues, pp. 328–333.
933
934 Tolosana-Delgado, R., McKinley, J. 2016. Exploring the joint compositional variability of major
935 components and trace elements in the Tellus soil geochemistry survey (Northern Ireland), Applied
936 Geochemistry (2016), http://dx.doi.org/10.1016/j.apgeochem.2016.05.004.
937